Anomaly patterns about strong convective events in the tropics and mid-latitudes: observations from radiosondes and surface weather stations

Toni Mitovski and Ian Folkins

Department of Physics and Atmospheric Science, Dalhousie University, Halifax, NS, Canada

Correspondence to T. Mitovski (mitovski@dal.ca)

Abstract

We use 13 years (1998 - 2010) of rainfall estimates from the Tropical Rainfall Measuring Mission (TRMM) 3B42 dataset to identify high rain events located close to radiosonde or surface weather stations. This is done in four regions: the Western Tropical Pacific, Tropical Brazil, Southeast China, and Southeast United States. We then construct composite anomaly patterns of a large number of variables about these high rain events. These variables include temperature, relative humidity, surface pressure, Convective Available Potential Energy (CAPE), geopotential height, mass divergence, relative vorticity, and potential vorticity. One motivation of this analysis is to identify regional differences in the interaction between strong convective events and the background atmosphere. We find, overall, that the changes in meteorological variables which occur during the evolution of strong convective events in mid-latitudes are similar to the changes that occur in the tropics. In mid-latitudes, however, strong convective events are associated with stronger anomalies in surface pressure and geopotential height, and exhibit a warm anomaly in the lower troposphere prior to peak rainfall. In the Southeast United States, the near surface layer of positive CAPE that occurs prior to high rain events is thicker than in the Western Tropical Pacific. In the two mid-latitude regions, the mid-level PV maximum that develops during the growth stage of high rain events acquires a downward tilt toward the surface during the decay stage, suggesting downward transport toward the surface. A conceptual model previously used to interpret the anomaly patterns of the 2-day equatorial wave [*Haertel and Kiladis*, 2004] is used to interpret the anomaly patterns associated with more general types of high rain events in the tropics.

1. Introduction

With some exceptions [*Cotton et al*., 1989; *DeMott et al*., 2007], most observationally based analyses of the anomaly patterns associated with strong convective events have been based on measurements over the tropical oceans. Here, we use routine radiosonde observations to construct composite anomaly patterns of a large number of meteorological variables about high rain events in four regions: the Western Tropical Pacific, Tropical Brazil, the Southeast United States, and Southeast China. This approach enables us to identify regional similarities and differences in the interaction between deep convection and the background atmosphere. The meteorological variables we analyze include temperature, relative humidity, column water vapor, Convective Available Potential Energy (CAPE), geopotential height, mass divergence, surface pressure, relative vorticity, and potential vorticity. We first use the Tropical Rainfall Measuring Missing (TRMM) 3B42 dataset to identify 2x2-degree grid cells in which the rain rate exceeds a particular threshold. We then look for radiosonde or surface measurements that are co-located, and within 48 hours, of the TRMM high rain events. To obtain better statistics, this procedure is repeated at many radiosonde stations, using a large number of rain events from 1998 to 2010. This approach has been previously followed using routine radiosonde profiles [*Sherwood and Wahrlich*, 1999; *Mitovski et al*., 2010], measurements from field campaigns [*Sobel et al*., 2004; *Mapes et al*., 2006; *DeMott et al*., 2007; *Mapes et al*., 2009], satellite data [*Zelinka and Hartmann*, 2009; *Masunaga*, 2012], and re-analysis data [*Benedict and Randall*, 2007; *Rapp et al*., 2011]. Some of the anomaly patterns shown in this paper, especially with respect to temperature and relative humidity anomaly patterns in the tropics, therefore reproduce well known relationships. However, radiosonde observations have not been used to directly calculate the anomaly patterns of other meteorological variables such as geopotential height and potential vorticity, or the vertical profile of CAPE in the boundary layer.

2. Datasets

2.1 Rainfall Data

The TRMM 3B42 gridded rainfall dataset is constructed from several satellite borne sensors. These include a precipitation radar, multichannel microwave radiometer, and visible and infrared sensors [*Kummerow et al*., 1998; *Liu et al*., 2012]. The data is available at 3-h temporal (centered at 00:00, 03:00, 06:00, 09:00, 12:00, 15:00, 18:00, and 21:00 UTC), and 0.25 x 0.25 degree horizontal resolution. We used TRMM 3B42 rainfall to identify high rain events between Jan 1998 and Dec 2010.

64 **2.2 Radiosonde Data**

65 The Integrated Global Radiosonde Archive (IGRA) dataset is stored at the National Climatic
66 Data Center (NCDC) [*Durre at al*., 2006]. We used data from 53 radiosonde locations from the
67 1998 – 2010 time period. The locations of these stations are shown as open squares in Figure 1**,** and
68 are located in four regions: 6 from the Western Tropical Pacific, 11 from Tropical Brazil, 19 from
69 the Southeast United States, and 17 from Southeast China. The soundings provide temperature and
70 relative humidity profiles at variable vertical resolution. Within the Southeast United States region,
71 there were on average 42 temperature and relative humidity measurements below 100 hPa. The
72 comparable numbers for the radiosonde stations in the Western Tropical Pacific, Tropical Brazil,
73 and Southeast China regions, are 39, 26, and 14, respectively. The soundings also provide
74 horizontal wind measurements at the surface and at the standard pressure levels of 1000, 925, 850,
75 700, 500, 400, 300, 250, 200, 150, and 100 hPa. Although some of the IGRA soundings are
76 available every 6 hours, the majority of the soundings are available twice per day at the 00:00 and
77 12:00 UTC standard synoptic times.

78 The divergence and vorticity anomaly calculations require simultaneous horizontal wind
79 measurements from triangular radiosonde arrays. For these variables, we used 2 arrays from the
80 Western Tropical Pacific, 5 arrays from Tropical Brazil, 14 arrays from the Southeast United States,
81 and 17 arrays from Southeast China. The average area of the Western Tropical Pacific arrays was
82 296,000 km^2 (roughly equal to the area of a 5x5-degree grid box at the equator), 57,000 km^2 for the
83 Southeast United States arrays (roughly equal to a 2.5x2.5-degree grid box at 30°N), 207,000 km^2
84 for the Tropical Brazil arrays, and 31,000 km^2 for the Southeast China arrays.

85

86 **2.3 Hourly Surface Data**

87 Over land, convective precipitation usually peaks in the late afternoon [*Nesbitt and Zipser*,
88 2003]. The rain events used to construct the anomaly patterns over land also occur more frequently
89 in the late afternoon. Within a given region, the radiosonde are usually launched at two fixed local
90 solar times. The incomplete diurnal sampling of the radiosondes, in combination with the existence
91 of diurnal cycles in both the rain event frequency and the meteorological variables, will introduce
92 biases into the calculation of our anomaly patterns. It is therefore important that, where possible, the
93 radiosonde anomaly patterns be validated against surface measurements with better temporal
94 resolution. The Integrated Surface Hourly (ISH) dataset consists of surface weather observations
95 from about 20,000 worldwide-distributed stations [*Lott et al*., 2001]. The data is archived at the
96 NCDC, and contains hourly and synoptic (3-hourly) surface weather observations of several
97 variables, including temperature, relative humidity, and pressure. We used ISH data between 1998

and 2010, from surface stations, which were co-located with the 53 IGRA radiosonde stations shown in Figure 1.

2.4 Global Positioning System Data

We used Global Positioning System (GPS) radio occultation temperature measurements from the Constellation Observing System for Meteorology, Ionosphere and Climate (COSMIC) six-satellite constellation [*Anthes et al*., 2008], downloaded from the COSMIC Data Analysis and Archive Center (CDAAC). There are approximately 2,000 high-vertical resolution (~100 m in the troposphere) COSMIC temperature profiles over the earth per day. Over a particular region, the COSMIC profiles are distributed roughly uniformly in local solar time. They can therefore also be used to help determine whether the calculated radiosonde temperature anomaly patterns over land exhibit a diurnal bias. We used COSMIC temperature profiles within the Southeast United States (between 30°N and 40°N and between 85°W and 100°W) and Southeast China (between 25°N and 35°N and between 103°E and 118°E) regions shown in Figures 1c and 1d. For both regions, we restricted attention to the convective summer season (June, July, and August) from 2006 to 2010.

3. Rain Event Definition

In the construction of the radiosonde and surface station anomaly patterns, high rain events were considered to occur at locations where the mean TRMM 3B42 rainfall over a 2 by 2 degree box centered at each station exceeded 1.5 mm/h over a TRMM 3-hour time interval. For the calculation of the mass divergence and relative vorticity anomaly patterns, we used triangular radiosonde arrays, and rain events were defined using the average TRMM 3B42 rain rate within each array. For the Southeast United States and Southeast China regions, we restricted attention to June, July, and August. For the tropical Brazil and the Western Tropical Pacific regions, we used rain events from the entire year.

Figure 2a shows the composite TRMM 3B42 2x2-degree mean rain event profiles from the four regions. The mean peak rain rate of close to 3 mm/h is significantly higher than the rain event threshold of 1.5 mm/h. The composite rain event profiles were constructed from events co-located with radiosonde or surface stations, rather than from rain events within the variably sized radiosonde arrays. The rain event profiles are quite similar to each other, partly reflecting the use of a common rain event threshold for all regions. High rain events develop slightly more rapidly over the three land regions than the Tropical Western Pacific. Rainfall starts to increase roughly 9 hours prior to peak rainfall and drops to near background levels roughly 9 hours after peak rainfall.

Within a particular region, the GPS COSMIC temperature profiles tend to be randomly distributed in space. In order to identify high rain events co-located with GPS temperature profiles, we first calculated the mean TRMM 3B42 rain rate in 2x2-degree grid boxes, separated from each other by 1 degree. For example, the Southeast United States region shown in Figure 1c enclosed an area between 30°- 40°N and 85°- 100°W. Within this region, we calculated the mean rain rate in 10 x 15 = 150 overlapping 2x2-degree grid boxes, and searched for GPS temperature profiles within each box. The Southeast China region shown in Figure 1d enclosed an area between 25°- 35°N and 103°- 118°E, and was also partitioned into 150 overlapping boxes.

Figure 2b shows the variation in average rain rate as a function of radial distance from the high rain events. The rain events of the various regions have a similar spatial scale, with the rain rate typically decaying to a near background value within about 400 km of peak rainfall.

4. Diurnal Variability

Figure 3a shows the average diurnal variation of the TRMM 3B42 rain rate within each of the four regions. As is well known [*Nesbitt and Zipser*, 2003], the rainfall rate within the three land regions peaks in the late afternoon or early evening. Within the Tropical Western Pacific region, the rainfall rate exhibits a small peak near 3 am. Figure 3b shows the diurnal variation in the frequency of occurrence of the rain events used to construct the radiosonde temperature anomaly patterns. The time of the diurnal peak in the rain event frequency is usually close to the time of the diurnal rainfall peak. The larger number of rain events within the Tropical Brazil region, despite the lower rain rate, is due to the use of rain events throughout the entire year, rather than June – August for the two mid-latitude regions.

Figure 4 shows the number of IGRA radiosonde profiles within each region that occurred within 48 hours of a rain event, and could therefore be used in the construction of the temperature anomaly patterns. Within the Southeast United States, there were approximately 21,000 profiles at 06 and 18 h local solar time available from the 1998 – 2010 time period. We used 25,000 profiles from Tropical Brazil (08 and 20 h local solar time), 55,000 profiles from Southeast China (also at 08 and 20 h local solar time), and roughly 80,000 soundings from the Tropical Western Pacific, distributed at local solar times of 00, 09, 10, 11, 12, 21, 22, and 23 h. The broader range of local solar times from the Tropical Western Pacific reflects the broader longitudinal distribution of the radiosonde stations in this region.

5. Results

164 **5.1 Temperature Anomaly Patterns From Radiosondes**

165 Once a rain event at a radiosonde station had been identified, we searched for radiosonde
166 launches that had occurred within 48 hours of the rain event. These soundings were then assigned to
167 3-h time bins, based on the difference between the radiosonde launch and rain event times. At each
168 location, the radiosonde measurements were used to define climatological temperature profiles for
169 each individual launch time, month, and year. These climatological profiles were then used to
170 convert the temperature profiles near high rain events to temperature anomaly profiles. We then
171 averaged the temperature anomaly profiles within each 3-h time bin.

172 The composite temperature anomaly patterns generated using the above procedure within
173 each region are shown in Figure 5a, 5b, 5c, and 5e. For all regions, high rain events are associated
174 with an upper-level warming centered at 300 hPa that is coincident with peak rainfall [*Cotton et al*.,
175 1989; *Sherwood and Wahrlich*, 1999; *Kiladis et al*., 2005; *Mapes et al*., 2006; *Mitovski et al*.,
176 2010]. With the exception of Southeast China, the regions also show a 700 hPa lower tropospheric
177 cooling coincident with peak rainfall. Each region shows a strong boundary layer cooling (below
178 900 hPa) after peak rainfall. This cooling is significantly larger and more persistent over the three
179 land regions than over the Tropical Western Pacific. Deep convection over the three land regions is
180 preceded by a warm anomaly in the lower troposphere. Over Tropical Brazil and Southeast China,
181 this warming extends upward from the surface to 800 hPa, but extends to 600 hPa over the
182 Southeast United States.

183 The details of the temperature anomaly patterns shown in Figure 5a, 5b, 5c, and 5e will be
184 sensitive, to some degree, to the assumptions used to define the rain events. For example, the use of
185 a larger rain event threshold would be expected to generate larger temperature anomalies. It has
186 been shown, however, that the shapes of the temperature anomaly patterns are not sensitive to the
187 value of the rain event threshold or the assumed event area [*Mitovski et al*., 2010].
188
189 **5.2 Temperature Anomaly Patterns From GPS**

190 The GPS COSMIC temperature profiles were used to also construct temperature anomaly
191 patterns of the Southeast United States and Southeast China regions. During the summer convective
192 season (JJA) between 2006 and 2010, there were 2,111 profiles from the United States, and 1,538
193 profiles from China, which were co-located within 48 hours of a TRMM rain event. The COSMIC
194 temperature anomaly patterns from these two regions are shown in Figure 5d and 5f. Although the
195 COSMIC and radiosonde temperature anomaly patterns are in good overall agreement, the
196 COSMIC boundary layer cooling is much smaller than the boundary layer cooling obtained from
197 the radiosonde data. There are several reasons why the COSMIC temperature anomaly patterns may

198 be less accurate near the surface. COSMIC provides vertical profiles of atmospheric refractivity,
199 which can be used to calculate the vertical profile of atmospheric density [*Anthes et al*., 2008].
200 Variations in water vapor can be expected to more strongly affect the atmospheric density at higher
201 temperatures closer to the surface. In the absence of an independent method of constraining the
202 water vapor profile, the relative accuracy of the COSMIC temperature retrievals can be expected to
203 be smaller at lower altitudes. The standard deviation of the difference between COSMIC and
204 radiosonde temperatures does increase toward the surface, though this does not appear to be
205 associated with an increase in the mean bias [*Sun et al.*, 2010]. The refractivity gradient at the top of
206 the boundary layer frequently exceeds the critical refraction, which can result in a systematic
207 negative refractivity bias in the radio occultations within the boundary layer [*Xie et al*., 2012].
208 Finally, the number of COSMIC temperature retrievals decreases toward the surface, especially for
209 altitudes below 2 km [*Anthes et al*., 2008].
210
211 **5.3 Anomalies in Pressure, Temperature, and Relative Humidity at the Surface**
212 Figure 6 shows the surface temperature, surface relative humidity, and surface pressure
213 anomalies during high rain events within each of the four regions, calculated from both the
214 radiosonde and surface weather station data. In general, the radiosonde anomaly profiles (solid
215 lines) are in good agreement with the profiles generated by higher temporal resolution surface
216 station measurements (dotted lines).
217 The top row of Figure 6 shows the surface temperature anomaly during high rain events. The
218 three land regions show larger surface cooling than the Tropical West Pacific region. This is
219 consistent with Figure 5, which also shows that the boundary layer cooling over land exhibits
220 greater persistence and depth. One explanation for this difference is that the relative humidity in the
221 lower troposphere over the three land regions tends to be smaller than the relative humidity in the
222 lower troposphere over the ocean region. Downdrafts over land would therefore be expected to
223 exhibit stronger negative buoyancies, have a higher probability of penetrating the boundary layer,
224 and possibly, generate more persistent cooling. It is also possible that, due to a weaker effective
225 heat capacity over land, the sensible heat flux from the surface in response to a cold anomaly near
226 the ground is likely to be weaker over land than the ocean.
227 The middle row of Figure 6 shows the anomaly in surface relative humidity during high rain
228 events. Within all four regions, convective rainfall is associated with a sharp increase in surface
229 relative humidity that is coincident, or slightly lags, peak rainfall. As would be expected, the size of
230 the relative humidity increase scales with the size of the temperature decrease, with the two mid-
231 latitude land regions exhibiting the largest increases in surface relative humidity.

The bottom row of Figure 6 shows the surface pressure anomalies during high rain events. These anomalies show larger regional differences than the temperature and relative humidity anomalies. In the Western Tropical Pacific, there is a 0.5 hPa minimum in surface pressure 10 hours prior to peak rainfall, followed by a small local maximum that slightly lags peak rainfall. In the Tropical Brazil region, there is a more rapid increase in surface pressure during high rain events. In the two mid-latitude regions, high rain events are associated with 1-2 hPa reductions in surface pressure over a 2-3 day timescale.

The surface pressure anomalies of the radiosonde stations within the Southeast United States, and to a lesser extent within Southeast China and Tropical Brazil, are significantly different from the surface pressure anomalies obtained from the surface stations. These deviations have a 12-hour periodicity. The black curve in Figure 7a shows the average diurnal cycle of the surface pressure anomaly for the Southeast United States surface stations. The red curve shows the diurnal cycle of the surface pressure anomaly, calculated using only those surface pressure measurements for which the rain rate of the local grid cell exceeded 1 mm/h. During the afternoon (14:00 – 18:00 local time), the presence of rainfall is not associated with deviations in surface pressure from the mean diurnal cycle. However, outside this afternoon and early evening time window, rainfall is associated with reduced surface pressure. Figure 7c shows that the surface pressure anomaly during high rain events depends on the time at which the rain event occurs. Each anomaly curve is constructed from high rain events having a common TRMM time, converted here to the approximate local solar time. The three curves with the largest negative anomalies in surface pressure are associated with rain events at 21:00 (solid green curve), 00:00 (solid blue curve), and 03:00 (solid red curve). The two anomaly curves with the smallest negative anomalies in surface pressure are associated with rain events which occur at 15:00 (dashed red curve) and 18:00 (solid black curve). This is consistent with Figure 7a. Rain events which occur during the late evening and early morning are associated with larger decreases in surface pressure (relative to the mean surface pressure at that local time) than rain events in the late afternoon.

The existence of a diurnal cycle in the magnitude of the surface pressure anomaly associated with high rain events leads to errors when the twice daily radiosonde profiles are used to construct the surface pressure anomaly patterns. The twice daily radiosonde launches occur at local solar times of 6 and 18 h. Figure 7b shows the surface pressure anomaly constructed from the individual sondes, as well as the combined response shown previously in Figure 6. For the two individual anomalies, there is a 24 h oscillation generated by changes in the local solar time of the rain events. For example, the curve generated using the 6 local time (LT) radiosonde launches and the curve generated using the 18 LT radiosonde launches both show maxima associated with rain events

occurring at 15 LT, and minima associated with rain events occurring at 00 LT. The anomaly pattern is consistent with Figure 7c, which shows weaker surface pressure anomalies for rain events in the late afternoon, and stronger surface pressure anomalies for rain events at night. The combined radiosonde surface pressure anomaly profile in Figure 7b, indicated by the dashed line, is equal to the average of the two individual radiosonde profiles, weighted by the relative frequency of the rain events used to construct the two profiles. Inspection of Figure 7b shows that the 12-hour oscillation in the combined radiosonde surface pressure anomaly pattern is an artifact generated from the 24-hour oscillations of the two individual curves. More generally, for variables which exhibit a coupling with convective precipitation which varies over the diurnal cycle, artifacts may be introduced when using 12 hourly radiosonde profiles to construct anomaly patterns in that variable.

5.4 Radial Distribution of the Convective Temperature Response

The temperature anomaly patterns shown in Figure 5 show the time evolution of the local temperature response to deep convection, but give no indication of the spatial scale over which these temperature anomalies extend. The radiosonde measurements can be used to calculate the vertical profile of the temperature anomaly as a function of the radial distance from the rain events. We first identified all 2x2-degree rain events within each of the regional boxes shown in Figure 1, and then searched for radiosonde measurements within 1000 km of the rain event which had occurred within 3 hours of the rain event time. The radiosonde temperature profiles were then stored in 50 km bins, based on the distance between the rain event and the radiosonde location. Each temperature profile was converted to an instantaneous anomaly profile by subtracting the climatological launch-time/monthly/yearly temperature profile at that location. The temperature anomaly profiles within each 50-km bin at each pressure level were then averaged, and the results shown in Figure 8**.**

The dominant feature of the radial temperature anomaly pattern is an upper level (300 hPa) warming that extends roughly 1000 km outward from the rain event. All four regions also exhibit a strong near surface (below 900 hPa) cooling that extends roughly 300 km outward from the rain event. The Western Tropical Pacific Ocean and Southeast United States regions also exhibit a strong lower tropospheric cooling between 800 hPa and 500 hPa. This lower tropospheric cooling is less pronounced over Tropical Brazil, and absent over Southeast China. The regional differences in the local convective temperature response shown in Figure 5 are therefore not restricted to the immediate environment of deep convective events, but extend to larger spatial scales.

5.5 Relative Humidity

The IGRA radiosonde dataset supplies vertical profiles of water vapor pressure, which can be converted to relative humidity. At temperatures below 0 °C, we normalized the vapor pressure by the saturation vapor pressure over ice [*Emanuel*, 1994]. In general, radiosonde measurements of vapor pressure are less accurate at colder temperatures [*Kley et al*., 2000]. The relative humidity was therefore not calculated for pressure levels above 200 hPa. Figure 9 shows the relative humidity response to high rain events, calculated using a procedure similar to that used for the temperature anomaly patterns. Within each region, peak rainfall is associated with values of relative humidity that exceed 80 % at most altitudes. The gradual moistening of the lower troposphere prior to high rain events has been attributed to the influence of congestus clouds [*Takayabu et al*., 1996; *Mapes et al*., 2006], but this interpretation has been recently challenged [*Hohenegger and Stevens*, 2013; *Masunaga*, 2013]. Rain events within the Southeast United States occur within a background atmosphere that is significantly drier than the other three regions, particularly in the upper troposphere.

5.6 Total Column Water Vapor Anomaly

The relative humidity and temperature measurements of the radiosonde profiles can be used to calculate the total column water vapor, defined here as the mass of water vapor per unit area between the surface and 200 hPa (also known as the precipitable water). Figure 10 shows the column water vapor anomaly during the growth and decay of high rain events within each region. Rain events in the Southeast United States occur at much lower values of column water than the other three regions (not shown). However, the change in column water during high rain events in the Southeast United States is very similar to the change in Southeast China and the Western Tropical Pacific (7-10 kg/m^2). Rain events in Tropical Brazil are associated with smaller increases in column water (less than 4 kg/m^2).

5.7 Convective Available Potential Energy

The existence of air parcels near the surface with positive Convective Available Potential Energy (CAPE) is a precondition for moist convection [*Sherwood and Wahrlich*, 1999]. We calculate CAPE by starting with air parcels near the surface whose pressure, temperature, and relative humidity are equal to the values given by a radiosonde profile at a particular pressure level. We lift the air parcel subject to the assumptions of constant moist static energy and total water (i.e. no condensate removal), no mixing, and no ice formation. Unfortunately, only the radiosonde

profiles of the Western Tropical Pacific and Southeast United States regions had sufficient vertical resolution to resolve the vertical structure of boundary layer CAPE.

The evolution of CAPE and the CAPE anomaly during the growth and decay of high rain events within these two regions is shown in Figure 11. In both regions, the decay stages of high rain events are associated with strongly negative CAPE anomalies which maximize near the surface several hours after peak rainfall. This CAPE reduction is presumably associated with some combination of preferential entrainment of higher moist static energy air parcels from the boundary layer by convective updrafts and by the injection of lower moist static energy air into the boundary layer from the mid-troposphere [*Zipser*, 1977; *Sherwood and Wahrlich*, 1999].

Figure 11 also shows that the near surface layer of positive CAPE is considerably thicker in the Southeast United States region than in the Western Tropical Pacific. Model simulations suggest that convective storms which grow from a deeper near surface moist layer, especially in the range of 1.5 – 2 km, can experience significantly less updraft dilution and develop stronger updraft speeds than those which grow from thinner moist layers [*McCaul and Cohen*, 2002]. In this case, Figure 11 may partially explain the well known fact that convective updrafts which occur over the ocean exhibit smaller updraft speeds than those which occur over land [*Lucas et al*., 1994], though other factors are probably also involved [*Robinson et al*., 2008].

Due to the diurnal cycle in CAPE over land [*Dai et al*., 1999], and the higher frequency of rain events during the late afternoon, some of the CAPE enhancement within the Southeast United States shown in Figure 11b prior to peak rainfall can be attributed to the diurnal cycle. The CAPE anomaly, in which the diurnal effect has been reduced by subtracting from each CAPE measurement the mean value of CAPE for each particular radiosonde launch time, station, and month is shown in Figures 11c and 11 d. Within the Western Tropical Pacific, there is very little change in CAPE prior to peak rainfall. Within the Southeast United States, the largest positive CAPE anomaly (~ 600 J/kg) occurs for parcels originating from 950 hPa roughly 6 hours prior to peak rainfall.

Figure 11 also shows that there is a 12 hour oscillation in the Southeast United States CAPE and CAPE anomaly patterns that mainly occurs prior to peak rainfall. This oscillation is an artifact generated by the same mechanism which produces the surface pressure oscillation shown in Figure 7. Although the top panel of Figure 6 shows that the surface temperature errors in the Southeast United States introduced by this sampling bias are small, these errors have a larger relative impact on CAPE.

365 **5.8 Geopotential Height**

366 Geopotential height profiles were calculated from the surface pressure, and temperature and
367 relative humidity profiles of individual radiosondes. The geopotential height at the surface of each
368 location was set equal to the local surface station altitude. We used stations whose altitude was less
369 than 200 m. We then iteratively calculated the geopotential height upward from the surface using
370 the hypsometric equation. This equation defines the geopotential height (GPHT) at a pressure level
371 n (p_n) in terms of the geopotential height at a lower pressure level n-1 (p_{n-1}), the virtual temperature
372 at levels n-1 ($T_{v,n-1}$) and n ($T_{v,n}$), and the pressure thickness dp.

373 $$GPHT_n = GPHT_{n-1} + R_d\left(\frac{T_{v,n-1} + T_{v,n}}{2g}\right)d\ln p. \qquad (1)$$

374 In this equation, p refers to pressure in Pascals, R_d to the specific gas constant of dry air (287.04
375 $Jkg^{-1}K^{-1}$), T_v to the virtual temperature of an air parcel, and g to standard gravity (9.806 ms^{-2}), and
376 dlnp is defined as

377 $$d\ln p = \frac{p_{n-1} - p_n}{0.5\left(p_{n-1} + p_n\right)}. \qquad (2)$$

378 To obtain the geopotential height anomaly, we subtracted from each geopotential height the
379 mean geopotential height for that station, month, and radiosonde launch time. We then grouped the
380 resulting geopotential height anomaly profiles of each region in 3-hour time bins about their
381 respective rain events. Figure 12 shows the geopotential height anomaly patterns associated with
382 the high rain events of each region. The anomaly pattern of the Southeast Unites States exhibits a
383 12 hour oscillation. This oscillation is stronger in the lower troposphere, and can be attributed to the
384 12 hour oscillation in lower tropospheric surface pressure discussed earlier.

385 The geopotential height anomaly patterns of the four regions show some common features.
386 Each region shows a strong positive geopotential height anomaly in the upper troposphere centered
387 at 200 hPa. This anomaly is generated mainly by the upper tropospheric 300 hPa warm anomaly
388 shown in Figure 5. Figure 12 also shows that the positive upper tropospheric geopotential height
389 anomalies within each region rapidly decrease above 200 hPa. This decrease with height can be
390 attributed to the intense narrow cold anomalies centered near 150 hPa shown in Figures 5 and 8,
391 which prevent the positive upper tropospheric geopotential height anomalies associated with strong
392 convective events from penetrating into the lower stratosphere [*Holloway and Neelin*, 2007].

393 In the two tropical regions, the negative mid-level geopotential anomaly is largest at 500 hPa,
394 and roughly symmetric about peak rainfall. The onset of negative geopotential height anomalies in
395 the lower tropospheric begins prior to the lower tropospheric cooling shown in Figure 5a, and can
396 be mainly attributed to local reductions in surface pressure. For example, the lower left panel of

Figure 6 shows that the surface pressure of the Western Tropical Pacific region decreases by roughly 0.6 hPa prior to peak rainfall. This would generate a geopotential height decrease of roughly 5.2 m, comparable with the lower tropospheric geopotential height anomalies prior to peak rainfall shown in Figure 12a.

In the two mid-latitude regions, negative surface pressure anomalies several days prior to peak rainfall contribute to negative geopotential height anomalies in the boundary layer. As peak rain rates develop, the cold anomalies in the boundary layer and mid-levels contribute to the intensification and upward extension of these negative geopotential height anomalies to 400 hPa. These negative mid-level geopotential height anomalies are much stronger, deeper, and more persistent than those observed in the tropics.

5.9 Mass Divergence

At a given pressure level, the net horizontal mass inflow or outflow from a convecting region can be estimated using horizontal wind measurements from radiosonde arrays. We calculated the mass divergence of the triangular arrays shown in Figure 1 using the following expression.

$$\nabla \cdot \vec{V} = \sum \frac{\vec{V} \cdot \vec{n} dl}{A} \qquad (3)$$

$V \cdot \vec{n}$ refers to the wind component normal with respect to a line that connects two points of the array, dl to the distance between the two points, and A to the surface area of the array.

The number of divergence profiles available to construct the anomaly patterns is usually much less than the number of available temperature or relative humidity profiles, partly because a divergence calculation require a complete ring of simultaneous horizontal wind measurements. The native resolution TRMM 3B42 dataset was used to calculate the average rainfall rate within the arrays shown in Figure 1. The rain event frequency is in general smaller for larger arrays. On average, there were 164 divergence profiles available per 3 h time bin from the two arrays in the Western Tropical Pacific, 205 profiles from the 14 arrays in the Southeast United States, 414 profiles from the 17 arrays in the Southeast China, and 102 profiles from the 5 arrays in the Equatorial Brazil.

Figure 13 shows the divergence anomaly patterns of each region. The four patterns are quite similar. The dominant feature of each pattern is a strong divergence maximum in the upper troposphere (200 hPa). This divergence maximum occurs near peak rainfall, but in three of the regions shows a tendency for stronger persistence after peak rainfall. Each region also shows a strong convergence feature in the boundary layer prior to peak rainfall, extending from the surface to 800 hPa. In the Western Tropical Pacific, this feature occurs 6 hours prior to peak rainfall. For

rain events within the three land regions, the time difference between the boundary layer divergence maximum and peak rainfall is roughly equal to 3 hours.

The divergence anomaly pattern of the Western Tropical Pacific region shown in Figure 13 exhibits an antisymmetric mid-level divergence dipole about peak rainfall [*Thompson et al*., 1979; *Mapes et al*., 2006; *Mapes et al*., 2009; *Mitovski et al*., 2010]. Within the three land regions, there is also a tendency for mid-level divergence to occur prior to peak rainfall and mid-level convergence to occur after peak rainfall. However, the timing of these divergence features is closer to peak rainfall than in the Western Tropical Pacific.

5.10 Relative Vorticity

Relative vorticity was calculated from the horizontal wind measurements of a radiosonde array using the following expression.

$$\zeta = \sum \frac{V_p dl}{A} \quad (4)$$

V_p refers to the wind component parallel to a line connecting two points in the array, dl to the distance between the two points, and A to the surface area of the array.

Unfortunately, the relative vorticity anomaly patterns of the two tropical regions were irregular and did not show strong features. This can probably be attributed to the weakness of the Coriolis parameter at the latitudes characteristic of the radiosonde arrays of these two regions, which would weaken the relative impact of the divergence term on the local vorticity budget. Figure 14a and 14b shows the relative vorticity anomaly patterns of the two mid-latitude regions. Within the Southeast China and Southeast United States regions, positive relative vorticity anomalies develop in the boundary layer one day prior to peak rainfall. These features are presumably associated with the coincident development of boundary layer convergence. At peak rainfall, the positive vorticity anomalies intensify and grow vertically to 400 hPa. The timing in the growth and vertical extent of these vorticity anomalies is consistent with the mid-level convergence features shown in Figure 13. Both regions also show a strong negative (anticyclonic) vorticity anomaly in the upper troposphere [*Cotton et al*., 1989], as would be expected to develop in response to the strong upper tropospheric outflow features shown in Figure 13.

5.11 Potential Vorticity

The production of Potential Vorticity (PV) within convective systems is believed to have a role in the development of the midlevel jet [*Franklin et al*., 2006]. PV was calculated from the temperature and horizontal wind profiles of the radiosonde arrays using then following expression.

$$PV = (\zeta + f)\left(-g\frac{\partial\theta}{\partial p}\right) \qquad (5)$$

In this equation, ζ refers to relative vorticity, f to the Coriolis parameter, g to standard gravity (9.806 ms^{-2}), θ to potential temperature, and p to pressure.

The PV and PV anomaly patterns about high rain events within the Southeast United States and Southeast China regions are shown in Figure 14c, 14d, 14e, and 14f, respectively. The tropopause is indicated by the strong vertical gradient in PV near 200 hPa. In both regions, high rain events are associated with strong negative PV anomalies near the tropopause. The development of this anomaly is consistent with a reduction in convective heating in going from the troposphere to the stratosphere.

Figures 14e and 14f also show that high rain events within the two regions are associated with positive PV anomalies that extend from the surface to 400 hPa. The stratiform type temperature response shown in Figures 5 and 8 would be expected to be associated with positive stability and PV anomalies in the mid-troposphere [*Hertenstein and Schubert*, 1991; *May et al*., 1994; *Franklin et al.,* 2006]. It has been shown that convective rainfall variability within the western half of the Southeast United States region shown in Figure 1c is modulated by PV anomalies generated along Rocky Mountains [*Li and Smith*, 2010]. This source of convective variability is likely to have some influence on the overall PV anomaly in this region. Figure 14e also shows that high rain events in the Southeast United States are also associated with strong positive PV anomalies near the surface. This increase is consistent with the increase in boundary layer stability that occurs during high rain events.

5.12 Tendencies

Figure 15a shows the relative humidity tendency about high rain events in the Western Tropical Pacific, calculated from the relative humidity anomaly pattern shown in Figure 9a. The tendency pattern is dominated by moistening during the growth stage of high rain events at all altitudes, but especially in the upper troposphere. During the decay stage, drying is strongest in the lower troposphere. Figure 15b shows the temperature tendency about high rain events in the Western Tropical Pacific, calculated from the temperature anomaly patterns shown in Figure 5a. The pattern is dominated by the development of a stratiform temperature response prior to peak rainfall, and the erosion of this response after peak rainfall.

Diagnostic interpretations of the anomaly patterns which occur during the evolution of strong convective events usually attribute the observed patterns to a combination of convective and large scale forcings [*Yanai et al*., 1973]. The large scale forcings refer, for example, to the

496 temperature and relative humidity tendencies associated with the mean vertical motion within a
497 radiosonde array and to horizontal advection. The convective forcings then refer to the sum of the
498 remaining physical tendencies which can not be attributed to the large scale flow. These include not
499 only the tendencies associated with moist convective circulations internal to the radiosonde array,
500 but also to the tendencies generated by other forms of turbulent mixing as well as radiative heating
501 and cooling. For a convective system, the particular partitioning of the observed (or residual)
502 tendency into large scale and convective components will depend on the size of the radiosonde
503 array used to diagnose the mean vertical velocity within the array.

504 Figure 15c shows the evolution of the domain averaged vertical motion (pressure velocity)
505 within the two Western Tropical Pacific radiosonde arrays shown in Figure 1. It was calculated
506 from the divergence anomaly pattern shown in Figure 13a, the climatological divergence profile of
507 each array, and by imposing the boundary condition $\omega = 0$ at the 100 hPa pressure level. During the
508 growth stage of high rain events, there is strong upward motion throughout the troposphere, with
509 somewhat larger ascent in the lower troposphere. After peak rainfall, the vertical motion is mainly
510 confined to the upper troposphere [*Mapes et al*., 2006]. Figure 15d shows the temperature tendency
511 pattern associated with the vertical motion pattern shown in Figure 15c, calculated by multiplying
512 the calculated pressure velocity by the appropriate static stability. The heating rate from the large
513 scale vertical motion appears to account for some features of the observed temperature tendencies.
514 In particular, the lower tropospheric warming after peak rainfall appears to be partially due to the
515 weakness of the lower tropospheric dynamical cooling during the decay stage of high rain events.
516
517 **6. Discussion in terms of two mode dynamical response**

518 Most of the rainfall variability in the Tropical West Pacific is associated with clusters of
519 enhanced convective activity propagating parallel to the equator and which have horizontal flows
520 similar to those exhibited by equatorially trapped shallow water waves [*Kiladis et al*., 2009]. One of
521 the more common wave types has a period of roughly 2 days, usually propagates westward with a
522 speed of 10 – 30 m/s, and is referred to as the 2-day wave [*Takayabu*, 1994]. The temperature,
523 divergence, and specific humidity anomaly patterns generated by these waves [*Kiladis et al*., 2009]
524 are similar to the anomaly patterns obtained here by averaging over all tropical high rain events.
525 The anomaly patterns of the 2-day waves can be reproduced by a simple model in which the
526 dynamical response to convective heating is dominated by two vertical modes [*Haertel and Kiladis*,
527 2004]. The first vertical mode is associated with upward or downward vertical motion which
528 extends throughout the troposphere, peaks at mid-levels, and can be mainly thought of as the
529 dynamical response to full depth convective heating. The dynamical heating from this mode is

roughly equal to the full depth convective heating, but almost exactly out of phase. As illustrated in Figure 16a, the full depth heating generated by deep convection is therefore almost exactly cancelled locally by the adiabatic cooling generated by the upward motion of the first mode. As a result, the induced subsidence heating and drying from deep convection is effectively exported to larger spatial scales.

The convective heating and induced vertical motion patterns associated the second vertical mode [*Haertel and Kiladis*, 2004] are illustrated in Figure 16c. During the growth stage of high rain events, there is convective warming in the lower troposphere (e.g. from cumulus congestus clouds), and convective cooling in the upper troposphere. The large scale upward motion in the lower troposphere and downward motion in the upper troposphere of mode 2 give rise to the observed mid-level divergence that occurs prior to peak rainfall, shown in Figure 13a. As with the first vertical mode, the heating tendencies associated with convection and the dynamical response oppose one another. However, because the magnitude of the dynamical heating exceeds the magnitude of the convective heating, the observed temperature tendency during the growth stage of high rain events is in phase with the dynamically induced cooling of the lower troposphere and the dynamical warming of the upper troposphere. After peak rainfall, the convective heating of the second mode is associated with convective cooling in the lower troposphere and convective warming in the upper troposphere (e.g. as would arise from precipitating stratiform anvil clouds). The induced dynamical motion is downward in the lower troposphere and upward in the upper troposphere, as required to generate the observed mid-level convergence. The magnitude of the dynamical heating again exceeds the magnitude of the convective heating, so that the net heating rate from the second mode is positive in the lower troposphere and negative in the upper troposphere, giving rise to the observed residual heating pattern which damps the stratiform temperature anomaly pattern generated during the growth stage of high rain events.

The net upward lower tropospheric motion of the second mode would favour moistening of the lower troposphere during the growth stage. Conversely, the net downward motion of the second mode would favour the drying of the lower troposphere during the decay stage. These effects are consistent with the observed relative humidity tendencies shown in Figure 15a. However, for the upper troposphere, it is not possible to interpret the observed relative humidity tendency in terms of the expected residual vertical motion of the second mode. This is particularly true during the growth stage where the upper troposphere warms (suggesting net descent), but the observed moistening is quite strong. This is presumably a reflection of the relatively greater role of detrained condensate in affecting the moisture budget of the upper troposphere.

In the above conceptual model [*Haertel and Kiladis*, 2004], the growth and decay of the dominant stratiform temperature response is attributed to an imbalance between the convective and dynamical heating of the second mode. It is not clear why the dynamical heating tendency of the second mode should be larger than that of the convective heating tendency. However, presumably, there is a self selection procedure whereby the size, propagation speed, and heating patterns of observed convective systems are self selected in ways that are favorable to their continued existence. This would include the rapid removal of the deep convective heating signature via the mode 1 dynamical response, so that the rainfall system continues to have sufficient CAPE, and the mid-level divergence during the growth stage, which would increase the column moist static energy [Haertel at al., 2008].

The mid-level divergence and associated upward lower tropospheric motion prior to peak rainfall would also promote the development of positive column water vapor anomalies during the growth stage of high rain events. Column water affects the growth of convective instabilities by modifying the effect of entrainment on updraft buoyancy [*Sherwood*, 1999; *Sherwood and Wahrlich*, 1999; *Raymond*, 2000]. For rain events in the Western Tropical Pacific, Figure 10 shows that column water starts to increase up to 48 hours prior to peak rainfall. This is much earlier than the onset of increases in rainfall (about 12 hours prior to peak rainfall), and suggests that the induced lower tropospheric uplift from the second mode may extend a considerable distance in front of a rain event. The radial temperature anomalies shown in Figure 8 support this viewpoint by showing that the lower tropospheric cold anomalies extend roughly 600 km outward from high rain events, again much larger than the size of the rain event itself. A slow synoptic scale rise in column water starting roughly 36 hours prior to peak rainfall also occurring prior to rainfall increases has been previously observed in other datasets [*Holloway and Neelin*, 2010].

The development of the stratiform temperature response during the growth stage of high rain events contributes to increases in mid-level stability and PV. During the decay stage, the net downward motion in the lower troposphere from the convective and large scale circulations (which contribute to the observed decrease in lower tropospheric relative humidity) would also be expected to transport the enhanced mid-level PV toward the surface. Although we could not calculate PV anomaly patterns of the two tropical regions, the PV patterns shown in Figure 14 for the Southeast United States and Southeast China regions give support for the existence of a tongue of higher PV air extending downward toward the surface from the 400 hPa level after peak rainfall. The downward advection of the mid-level PV maximum after peak rainfall may play a role in hurricane genesis. In the "top down" theory of hurricane genesis [*Gjorgjievska and Raymond*, 2013], a mid-level positive PV anomaly generated by the stratiform heating profile of a mesoscale convective

system is advected toward the surface by evaporative cooling, where it then initiates the formation of a warm core anticyclone [*Bister and Emanuel*, 1997].

7. Summary

We have used the TRMM 3B42 gridded rainfall dataset to identify 2x2-degree rain events in four regions: the Western Tropical Pacific, Tropical Brazil, Southeast China, and Southeast United States. Within each region, we selected rain events in close proximity to radiosonde or surface weather stations. These measurements were then used to construct composite anomaly patterns of a large number of meteorological variables about high rain events. One motivation of this analysis was to determine the regional similarities and differences in the interaction between strong convective events and the background atmosphere. The second motivation was to help determine the pathways by which the atmosphere returns to a balanced state following moist convection, and to help understand how these pathways affect the evolution of convective systems.

Our analysis shows that there are many similarities in the interaction between strong convective events and the background atmosphere between the four different regions. With the partial exception of Southeast China (which appears to lack the 700 hPa cooling maximum), deep convection occurs in association with the development of a stratiform type temperature response in the background atmosphere. In all four regions, the upper tropospheric warming extends roughly 1000 km outward from deep convective events, while the lower tropospheric cooling extends roughly 600 km. The upper tropospheric warming and lower tropospheric cooling generate increased stability at mid-levels. The mid-level stability increase can be expected to enhance convective detrainment in the mid-troposphere and promote the development of cumulus congestus clouds. High rain events in each of the four regions are associated with strong boundary layer cooling during the decay stage. This boundary layer cooling was stronger in the three land regions than in the Western Tropical Pacific.

In two of the four regions, we were able to calculate the time evolution of the vertical structure of CAPE in the boundary layer during high rain events. In agreement with previous studies [*Sherwood and Wahrlich*, 1999] the boundary layer cooling after peak rainfall contributes to the development of strongly negative CAPE anomalies throughout the boundary layer in both regions. Within the Southeast United States region, the CAPE enhancement prior to peak rainfall was roughly 200 J/kg. The near surface layer of positive CAPE was much deeper over land than the ocean. Within the Southeast United States region, the positive CAPE layer extended to roughly 800 hPa, whereas within the Western Tropical Pacific region it extended to only 900 hPa.

There were regional variations in the interaction between strong convective events and the background atmosphere. In the two mid-latitude regions, the mid and lower tropospheric negative geopotential height anomalies that developed during and after high rain events were much stronger, more vertically coherent, and more persistent than in the two tropical regions. These more strongly negative geopotential height anomalies can be partly attributed to the more strongly negative surface pressure anomalies that develop during mid-latitude convection. An additional difference is that each of the three land regions exhibited warming in the lower troposphere prior to peak rainfall, a feature absent from the tropical ocean region. Finally, the mid-level stratiform convergence of the two mid-latitude regions occurred closer in time to peak rainfall than in the two tropical regions.

Within the Southeast United States region, rain events which occur during the evening are associated with larger reductions in surface pressure than those which occur during the day. It is not clear whether the larger surface pressure reductions at night were driven by a diurnal change in the nature of deep convection, or whether the larger surface pressure reduction at night is associated with more strongly forced synoptic environments for convective events. However, if convection does indeed force the larger nighttime surface pressure reductions, diurnal changes in behavior of deep convection may contribute to the observed diurnal cycle of surface pressure in this region.

Convective circulations modify the temperature, relative humidity, and surface pressure of the background atmosphere, and contribute to the generation of geopotential height anomalies. These geopotential height anomalies, in concert with any pre-existing dynamical forcings, contribute to the large scale circulations which occur in association with convective events. The observed anomaly patterns therefore result from both the direct effects of convection and the large scale flow. We have suggested that a two mode dynamical model originally developed to explain the anomaly patterns of the 2-day wave [*Haertel and Kiladis*, 2004], and later used to interpret anomalies associated with the Madden-Julian oscillation [*Haertel et al*., 2008], is an appropriate conceptual model for interpreting the mean anomaly patterns of high rain events over the tropical oceans. In this model, the negative mid-level geopotential height anomalies that develop during the growth stage of convective events help drive a convergent mid-level inflow toward high rain events during the decay stage that requires, by mass balance, compensatory lower tropospheric uplift in the background atmosphere. This uplift appears to be responsible for the development of positive column water vapor anomalies which develop up to 48 hours prior to peak rainfall, and roughly 36 hours prior to the onset of increases in rain rate.

We were able to calculate the vorticity and potential vorticity anomaly patterns of high rain events in the Southeast China the Southeast United States regions. In both of these regions, high rain events are associated with negative anomalies in both upper tropospheric relative and potential

vorticity which extend into the lower stratosphere. Below 400 hPa, convective events are associated with positive anomalies in relative vorticity and potential vorticity. During the decay stage of high rain events, the mid-level positive PV anomaly appears to be transported toward the surface by the net downward circulation.

Acknowledgements

The author acknowledges useful discussions with Glen Lesins and Randall Martin. Comments and suggestions by three anonymous reviewers greatly improved the manuscript. We thank the following institutions for making their data public: NASA GSFC (TRMM 3B42), NCDC (IGRA and ISH) and NCAR UCAR (COSMIC). This research was supported by a Research Grant from the Natural Sciences and Engineering Council of Canada.

References

Anthes, R. A., and Coauthors (2008), The COSMIC/FORMOSAT-3 Mission: Early Results. *Bull. Amer. Meteor. Soc.*, **89**, 313–333, doi:10.1175/BAMS-89-3-313.

Benedict, J., and D. A. Randall (2007), Observed characteristics of the MJO relative to maximum rainfall. *J. Atmos. Sci*., **64**, 2332-2354, doi:10.1175/JAS3968.1.

Bister, M., and K. A. Emanuel (1997), The genesis of Hurricane Guillermo: TEXMEX analyses and a modeling study. *Mon. Wea. Rev*., **125**, 2662-2682, doi:10.1175/1520-0493(1997)125<2662:TGOHGT>2.0.CO;2.

Cotton, W. R., M-S. Lin, R. L. McAnelly, and C. J. Tremback (1989), A composite model of mesoscale convective complexes. *Mon. Wea. Rev.*, **117**, 765–783. doi: http://dx.doi.org/10.1175/1520-0493(1989)117<0765:ACMOMC>2.0.CO;2.

Dai, A., F. Giorgi, and K. E. Trenberth (1999), Observed and model-simulated diurnal cycles of precipitation over the contiguous United States. *J. Geophys. Res.,* **104**, 6377-6402, doi:10.1029/98JD02720.

DeMott, C., D. A. Randall, and M. Khairoutdinov (2007), Convective precipitation variability as a tool for general circulation model analysis. *J. Climate,* **20**, 91-112, doi:10.1175/JCLI3991.1.

Durre, I., R. S. Vose, and D. B. Wuertz (2006), Overview of the integrated global radiosonde archive. *J. Climate,* **19**, 53-68, doi:10.1175/JCLI3594.1.

Emanuel, K.A. (1994), *Atmospheric Convection*, Oxford University Press, New York, 580 pp.

Franklin, C. N., G. J. Holland, and P. T. May (2006), Mechanisms for the generation of mesoscale vorticity features in tropical cyclone rainbands. *Mon. Wea. Rev*., **134**, 2649–2669. doi: http://dx.doi.org/10.1175/MWR3222.1.

Gjorgjievska, S. and D. J. Raymond (2013), Interaction between dynamics and thermodynamics during tropical cyclogenesis. *Atmos. Chem. Phys*. *Discuss.*, **13**, 18905-18950, 2013. doi:10.5194/acpd-13-18905-2013

Haertel, P. T. and G. N. Kiladis (2004), Dynamics of 2-day equatorial waves. *J. Atmos. Sci.*, **61**, 2707–2721. doi: http://dx.doi.org/10.1175/JAS3352.1.

Haertel, P. T., G. N. Kiladis, A. Denno, and T. M. Rickenbach (2008), Vertical-mode decompositions of 2-day waves and the Madden–Julian oscillation. *J. Atmos. Sci.*, **65**, 813–833. doi: http://dx.doi.org/10.1175/2007JAS2314.1.

Hertenstein, R. F. A., and W. H. Schubert (1991), Potential vorticity anomalies associated with squall lines. *Mon. Wea. Rev*., **119**, 1663–1672, doi:10.1175/1520-0493(1991)119<1663:PVAAWS>2.0.CO;2.

Hohenegger, C., and B. Stevens (2013), Preconditioning deep convection with cumulus congestus. *J. Atmos. Sci*., **70**, 448–464, doi:10.1175/JAS-D-12-089.1.

Holloway, C. E. and J. D. Neelin (2007), The convective cold top and quasi equilibrium*. *J. Atmos. Sci.*, **64**, 1467–1487. doi: http://dx.doi.org/10.1175/JAS3907.1.

Holloway, C. E. and J. D. Neelin (2010), Temporal relations of column water vapor and tropical precipitation. *J. Atmos. Sci.*, **67**, 1091–1105. doi: http://dx.doi.org/10.1175/2009JAS3284.1.

Kiladis, G. N., K. H. Straub, and P. T. Haertel (2005), Zonal and vertical structure of the Madden–Julian oscillation. *J. Atmos. Sci.*, **62**, 2790–2809. doi: http://dx.doi.org/10.1175/JAS3520.1.

Kiladis, G. N., M. C. Wheeler, P. T. Haertel, K. H. Straub, and P. E. Roundy (2009), Convectively coupled equatorial waves. *Rev. Geophys*., **47**, RG2003, doi:10.1029/2008RG000266.

Kley, D., J. M. Russell III, and C. Phillips (Eds.) (2000), SPARC Assessment of upper tropospheric and stratospheric water vapor, WMO/TD-143, World Clim. Res. Programme, Geneva.

Kummerow, C., W. Barnes, T. Kozu, J. Shiue, and J. Simpson (1998), The Tropical Rainfall Measuring Mission (TRMM) sensor package. *J. Atmos. Oceanic Technol.,* **15**, 809-817, doi:10.1175/1520-0426(1998)015<0809:TTRMMT>2.0.CO;2.

723 Li, Y., and R. B. Smith (2010), The detection and significance of diurnal pressure and potential
724 vorticity anomalies east of the Rockies. *J. Atmos. Sci.*, **67**, 2734–2751. doi:
725 http://dx.doi.org/10.1175/2010JAS3423.1.
726 Liu, Z., D. Ostrenga, W. Teng, and S. Kempler (2012), Tropical Rainfall Measuring Mission
727 (TRMM) precipitation data and services for research and applications. *Bull. Amer. Meteor. Soc.,*
728 **93**, 1317-1325, doi:10.1175/BAMS-D-11-00152.1.
729 Lott, N., R. Baldwin, and P. Jones (2001), The FCC integrated surface hourly database: A new
730 resource of global climate date. NOAA National Climatic Data Center Tech. Rep. 2001-01, 42
731 pp.
732 Lucas, C., E. J. Zipser, and M. A. Lemone (1994), Vertical velocity in oceanic convection off
733 tropical Australia. *J. Atmos. Sci.*, **51**, 3183–3193. doi: http://dx.doi.org/10.1175/1520-
734 0469(1994)051<3183:VVIOCO>2.0.CO;2
735 Mapes, B. E., S. Tulich, J. Lin, and P. Zuidema (2006), The mesoscale convection life cycle:
736 Building block or prototype for large-scale tropical waves? *Dyn. Atmos. Oceans,* **42**, 3-29,
737 doi:10.1016/j.dynatmoce.2006.03.003.
738 Mapes, B. E., et al. (2009), Virtual field campaigns on deep tropical convection in climate models.
739 *J. Climate*, **22**, 244–257, doi:10.1175/2008JCLI2203.1.
740 Masunaga, H. (2012), A satellite study of the atmospheric forcing and response to moist convection
741 over tropical and subtropical oceans. *J. Atmos. Sci*., **69**, 150–167, doi:10.1175/JAS-D-11-016.1.
742 Masunaga, H. (2013), A satellite study of tropical moist convection and environmental variability:
743 A moisture and thermal budget analysis. *J. Atmos. Sci.*, **70**, 2443–2466. doi:
744 http://dx.doi.org/10.1175/JAS-D-12-0273.1.
745 May, P. T., G. J. Holland, and W. L. Ecklund (1994), Wind profiler observations of tropical storm
746 Flo at Saipan. *Wea. Forecasting*, **9**, 410–426. doi: http://dx.doi.org/10.1175/1520-
747 0434(1994)009<0410:WPOOTS>2.0.CO;2.
748 McCaul, E. W., and C. Cohen (2002), The impact on simulated storm structure and intensity of
749 variations in the mixed layer and moist layer depths. *Mon. Wea. Rev.*, **130**, 1722–1748. doi:
750 http://dx.doi.org/10.1175/1520-0493(2002)130<1722:TIOSSS>2.0.CO;2.
751 Mitovski, T., I. Folkins, K. von Salzen, and M. Sigmond (2010), Temperature, relative humidity,
752 and divergence response to high rainfall events in the tropics: Observations and models. *J.*
753 *Climate,* **23**, 3613-3625, doi:10.1175/2010JCLI3436.1.
754 Nesbitt, S. W., and E. J. Zipser (2003), The diurnal cycle of rainfall and convective intensity
755 according to three years of TRMM measurements. *J. Climate*, **16**, 1456–1475,
756 doi:10.1175/1520-0442-16.10.1456.
757 Rapp, A. D., C. Kummerow, and L. D. Fowler (2011), Interactions between warm rain clouds and
758 atmospheric preconditioning for deep convection in the tropics. *J. Geophys. Res*., **16**, D23210
759 doi:10.1029/2011JD016143.
760 Raymond, D. (2000), Thermodynamic control of tropical rainfall. *Quart. J. Roy. Meteor. Soc*., **126**,
761 889–898. doi: 10.1002/qj.49712656406.
762 Robinson, F. J., S. C. Sherwood, and Y. Li (2008), Resonant response of deep convection to surface
763 hot spots. *J. Atmos. Sci.*, **65**, 276–286. doi: http://dx.doi.org/10.1175/2007JAS2398.1.
764 Sherwood, S. C. (1999), Convective precursors and predictability in the Tropical Western Pacific.
765 *Mon. Wea. Rev.*, **127**, 2977–2991. doi: http://dx.doi.org/10.1175/1520-
766 0493(1999)127<2977:CPAPIT>2.0.CO;2.
767 Sherwood, S. C., and R. Wahrlich (1999), Observed evolution of tropical deep convective events
768 and their environment. *Mon. Wea. Rev.,* **127**, 1777-1795, doi:10.1175/1520-
769 0493(1999)127<1777:OEOTDC>2.0.CO;2.
770 Sobel, A. H., S. E. Yuter, C. S. Bretherton, and G. N. Kiladis (2004), Large-scale meteorology and
771 deep convection during TRMM KWAJEX. *Mon. Wea. Rev.,* **132**, 422–444, doi:10.1175/1520-
772 0493(2004)132<0422:LMADCD>2.0.CO;2.

773 Sun, B., A. Reale, D. J. Seidel, and D. C. Hunt (2010), Comparing radiosonde and COSMIC
774 atmospheric profile data to quantify differences among radiosonde types and the effects of
775 imperfect collocation on comparison statistics, *J. Geophys. Res.*, **115**, *D23104,*
776 *doi:*10.1029/2010JD014457.
777 Takayabu, Y. N. (1994), Large-scale cloud disturbances associated with equatorial waves. Part II:
778 Westward-propagating inertio-gravity waves. *J. Meteor. Soc. Japan*, **72**, 451–465.
779 Takayabu, Y. N., K.-M. Lau, and C.-H. Sui (1996), Observation of a quasi 2-day wave during
780 TOGA COARE. *Mon. Wea. Rev.,* **124**, 1892-1913, doi: 10.1175/1520-
781 0493(1996)124<1892:OOAQDW>2.0.CO;2.
782 Thompson, R. M., Jr., S. W. Payne, E. E. Recker, and R. J. Reed (1979), Structure and properties of
783 synoptic-scale wave disturbances in the intertropical convergence zone of the eastern Atlantic. *J.*
784 *Atmos. Sci.,* **36**, 53-72, doi:10.1175/1520-0469(1979)036<0053:SAPOSS>2.0.CO;2.
785 Xie, F., Wu, D. L., Ao, C. O., Mannucci, A. J., and Kursinski, E. R. (2012), Advances and
786 limitations of atmospheric boundary layer observations with GPS occultation over southeast
787 Pacific Ocean. *Atmos. Chem. Phys*., **12**, 903-918, doi:10.5194/acp-12-903-2012.
788 Yanai, M., S. Esbensen, and J.-H. Chu (1973), Determination of bulk properties of tropical cloud
789 clusters from large-scale heat and moisture budgets. *J. Atmos. Sci*., **30**, 611–627. doi:
790 http://dx.doi.org/10.1175/1520-0469(1973)030<0611:DOBPOT>2.0.CO;2.
791 Zelinka, M. D., and D. L. Hartmann (2009), Response of humidity and clouds to tropical deep
792 convection. *J. Climate*, **22**, 2389–2404. doi: http://dx.doi.org/10.1175/2008JCLI2452.1.
793 Zipser, E. J. (1977), Mesoscale and convective-scale downdrafts as distinct components of a squall-
794 line structure. *Mon. Wea. Rev*., **105**, 1568 – 1589, doi:10.1175/1520-
795 0493(1977)105<1568:MACDAD>2.0.CO;2.

Figure Captions

Figure 1. Open squares refer to the co-located IGRA radiosonde station and the ISH weather stations used to construct the anomaly patterns. The triangles show the radiosonde arrays used to calculate the mass divergence, relative vorticity, and potential vorticity anomaly patterns. The large rectangles show the regions within which rain events were chosen to calculate the radial variation of temperature about high rain events.

Figure 2. (a) The variation in mean rainfall during the growth and decay of the TRMM 3B42 2x2-degree high rain events within each region. (b) The radial variation in mean rainfall about the high rain events.

Figure 3. (a) The variation in TRMM 3B42 2x2-degree rainfall with local solar time, averaged over the radiosonde locations of each region shown in Figure 1. (b) The diurnal variation in the number of high rain events within each 3-hour time bin, calculated from all rain events used in the construction of the temperature anomaly patterns.

Figure 4. The number of available soundings, at each local solar time, within 48 hours of the rainfall events used in the construction of the temperature anomaly patterns. Different colors refer to different regions.

Figure 5. (a), (b), (c), and (e) show temperature anomaly patterns about the TRMM high rain events, calculated using IGRA radiosonde profiles from each region. (d) and (f) show temperature anomaly patterns calculated using the COSMIC GPS temperature profiles.

Figure 6. Within each figure, the dotted line refers to an anomaly profile calculated using 1-h ISH surface data, while the solid lines refer to anomaly profiles calculated using 12-h IGRA radiosonde data. (upper row) The variation of the surface temperature anomaly during high rain events. (middle row) The variation of surface relative humidity anomaly during high rain events. (bottom row) The variation in the surface pressure anomaly during high rain events. Each column refers to a different region with from left to right: the Tropical Western Pacific, Tropical Brazil, Southeast USA, and Southeast China regions.

Figure 7. (a) The black curve of the top panel shows the diurnal variation in the surface pressure anomaly, plotted against local solar time, of the surface stations within the Southeast United States region shown in Figure 1 (June, July, and August). The red curve was obtained from the subset of surface pressure measurements at which the local rain rate of each surface station exceeded 1.0 mm/h; (b) The solid black curve shows the surface pressure anomaly about high rain events constructed using radiosonde measurements launched at 6 LT only. The red curve shows the surface pressure anomaly about high rain constructed from radiosonde measurements at 18 LT only. The black dashed line shows the combined surface pressure anomaly of the two radiosonde launch times. (c) Each curve shows the surface pressure response, calculated using ISH surface station data within the Southeast United States region, to TRMM rain events occurring at a particular time. For each curve, the local time of the TRMM rain events is shown in the legend. The circles in the middle panel indicate the local time of the rain events about which the pressure anomaly was calculated. For example, the red circles of the middle panel indicate surface pressure anomalies calculated from radiosondes launched at 18 LT, from rain events at 15 LT. Each red circle of the middle panel corresponds to a red circle in the lower panel, which indicates the effect of rain occurring events at that time on the surface pressure anomaly. In general, maxima in the curves of the middle panel occur at times when the corresponding rain events are associated with a smaller surface pressure anomaly, and vice versa.

847

848 Figure 8. The radial distribution of the temperature anomaly about high rain events in each region.
849 The horizontal axis refers to the radial distance between a radiosonde location and a TRMM high
850 rain event. The patterns were constructed from radiosonde launches within 3 h of a TRMM rain
851 event.

852

853 Figure 9. The variation in relative humidity during the evolution of high rain events in each region.
854 The horizontal axis refers to time since peak rainfall.

855

856 Figure 10. The variation of the total column water vapor anomaly about high rain events in each
857 region. The total column water vapor anomaly is a mass weighted vertical integral of the specific
858 humidity anomaly between 1000 and 200 hPa, as measured by a radiosonde profile.

859

860 Figure 11. Panels (a) and (b) show the variation in boundary layer CAPE during high rain events in
861 the Western Tropical Pacific and Southeast United States regions. The horizontal axis refers to time
862 since peak rainfall. Panels (c) and (d) are similar to the upper panels, but show the CAPE anomaly.

863

864 Figure 12. The variation in geopotential height (GPHT) during high rain events in each region. The
865 horizontal axis refers to time since peak rainfall.

866

867 Figure 13. The variation in the mass divergence anomaly during high rain events in each region.
868 The horizontal axis refers to time since peak rainfall.

869

870 Figure 14. Panels (a) and (b) show the variation in the relative vorticity anomaly about high rain
871 events, calculated from radiosonde arrays in the Southeast United States and China. Panels (c) and
872 (d) show the variation in Potential Vorticity (PV) about high rain events. Panels (e) and (f) show the

873 variation in the potential vorticity anomaly about high rain events. The horizontal axis refers to time
874 since peak rainfall. The potential vorticity is expressed in potential vorticity units (PVU), where 1
875 PVU $= 10^{-6} m^2 s^{-1} K kg^{-1}$.
876
877 Figure 15. (a) The relative humidity tendency pattern (dRH/dt) calculated from the Western
878 Tropical Pacific relative humidity pattern shown in Figure 9a. (b) The observed temperature
879 tendency pattern (dT/dt), calculated from the Western Tropical Pacific temperature anomaly
880 patterns shown in Figure 5a. (c) The vertical pressure velocity calculated from the Western Pacific
881 divergence anomaly pattern shown in Figure 13a. (d) The temperature tendency pattern due to
882 vertical advection, calculated from the vertical pressure velocity and stability anomaly patterns.
883
884 Figure 16. (a) The top panel shows the convective heating and large scale circulation associated
885 with mode 1. The convective heating is indicated with the red oval, and the large-scale dynamical
886 motions by the arrows. (b) Rainfall and column water anomalies about high rain events in Western
887 Tropical Pacific region. (c) The convective heating and large scale circulations associated with
888 mode 2. Dark blue and red ovals show observed cold and warm temperature anomalies. This figure
889 has been adapted and modified from Figure 10 of Haertel and Kiladis [2004].

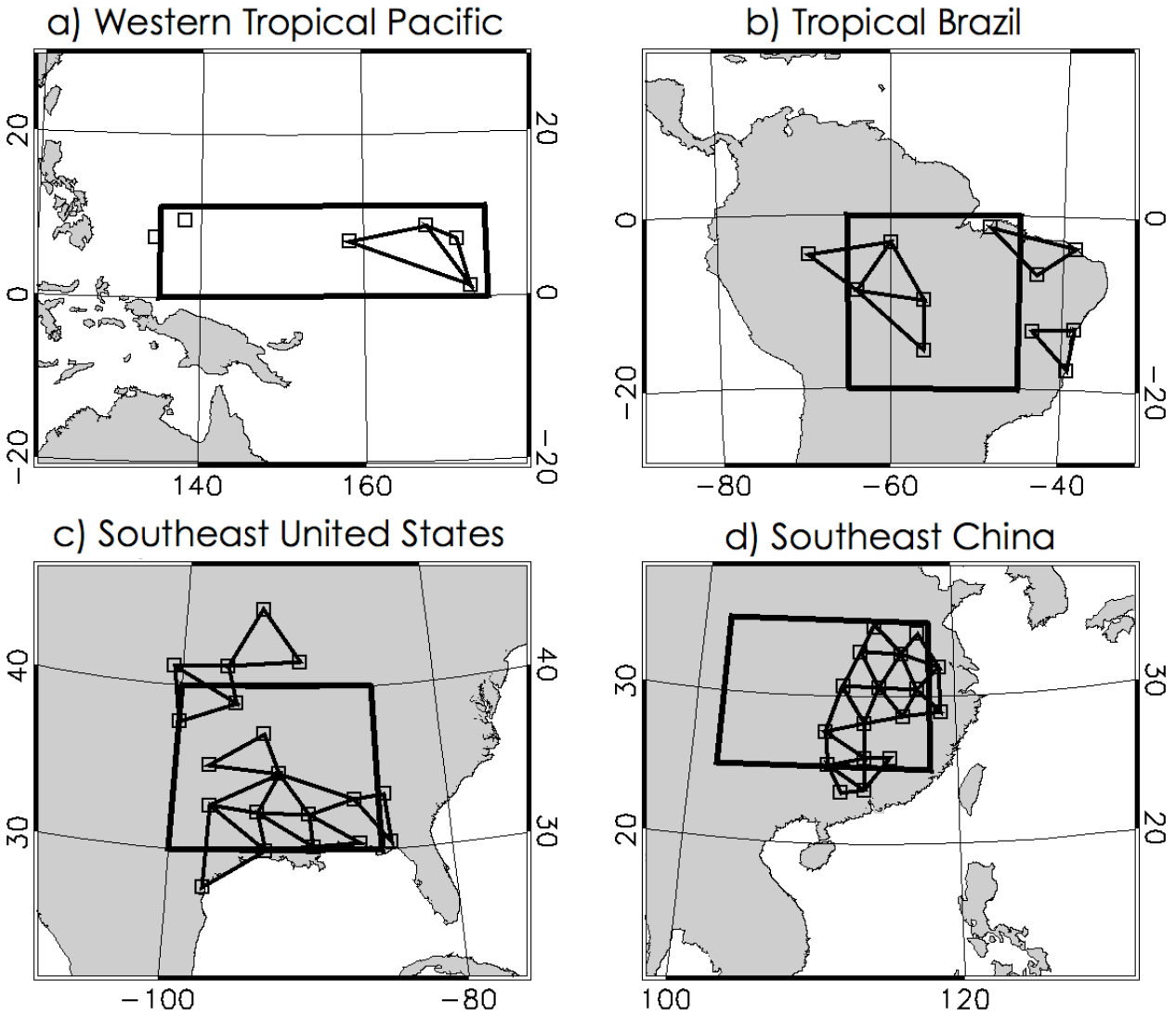

Figure 1. Open squares refer to the co-located IGRA radiosonde station and the ISH weather stations used to construct the anomaly patterns. The triangles show the radiosonde arrays used to calculate the mass divergence, relative vorticity, and potential vorticity anomaly patterns. The large rectangles show the regions within which rain events were chosen to calculate the radial variation of temperature about high rain events.

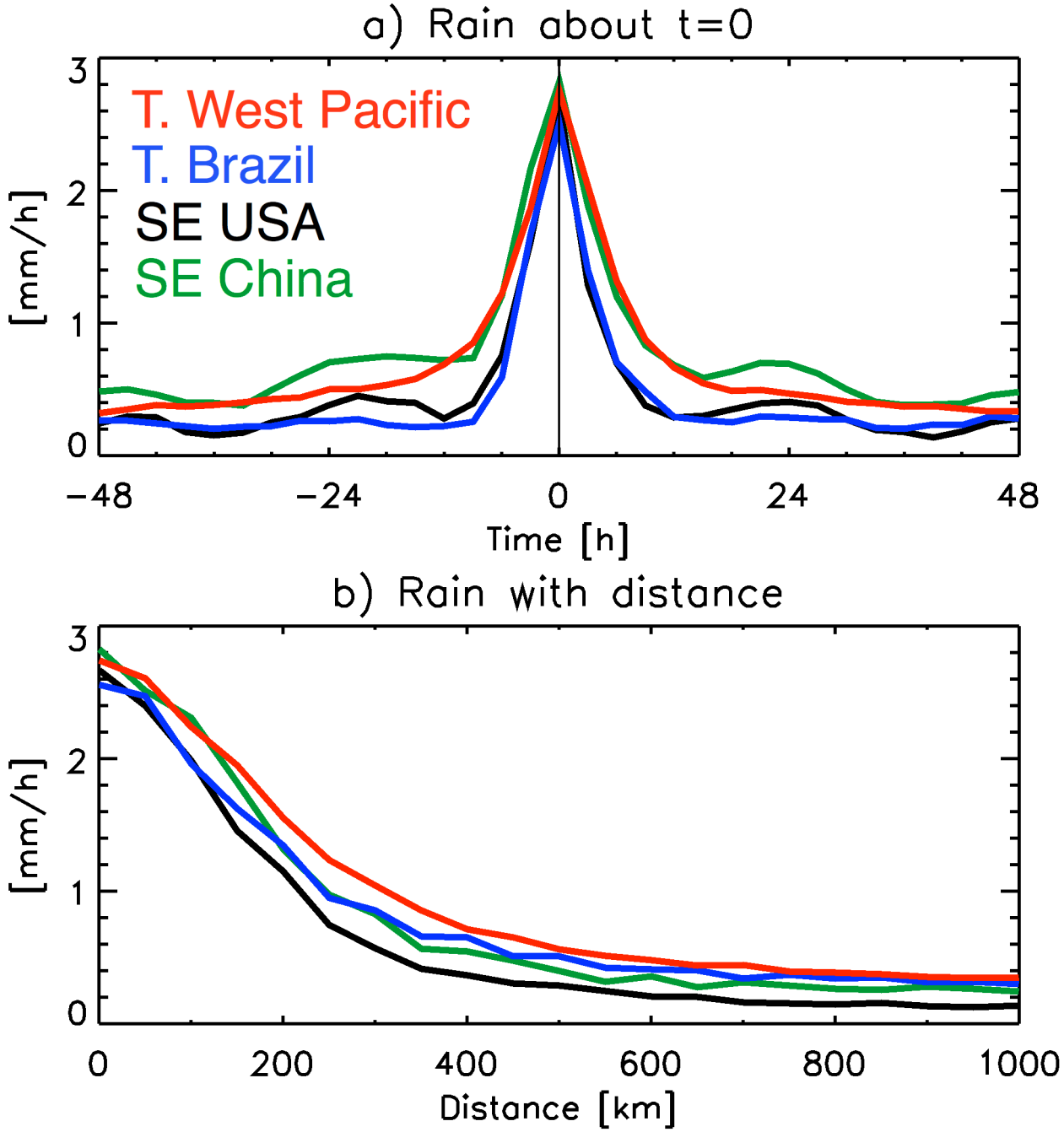

898

899 Figure 2. (a) The variation in mean rainfall during the growth and decay of the TRMM 3B42 2x2-
900 degree high rain events within each region. (b) The radial variation in mean rainfall about the high
901 rain events.

902

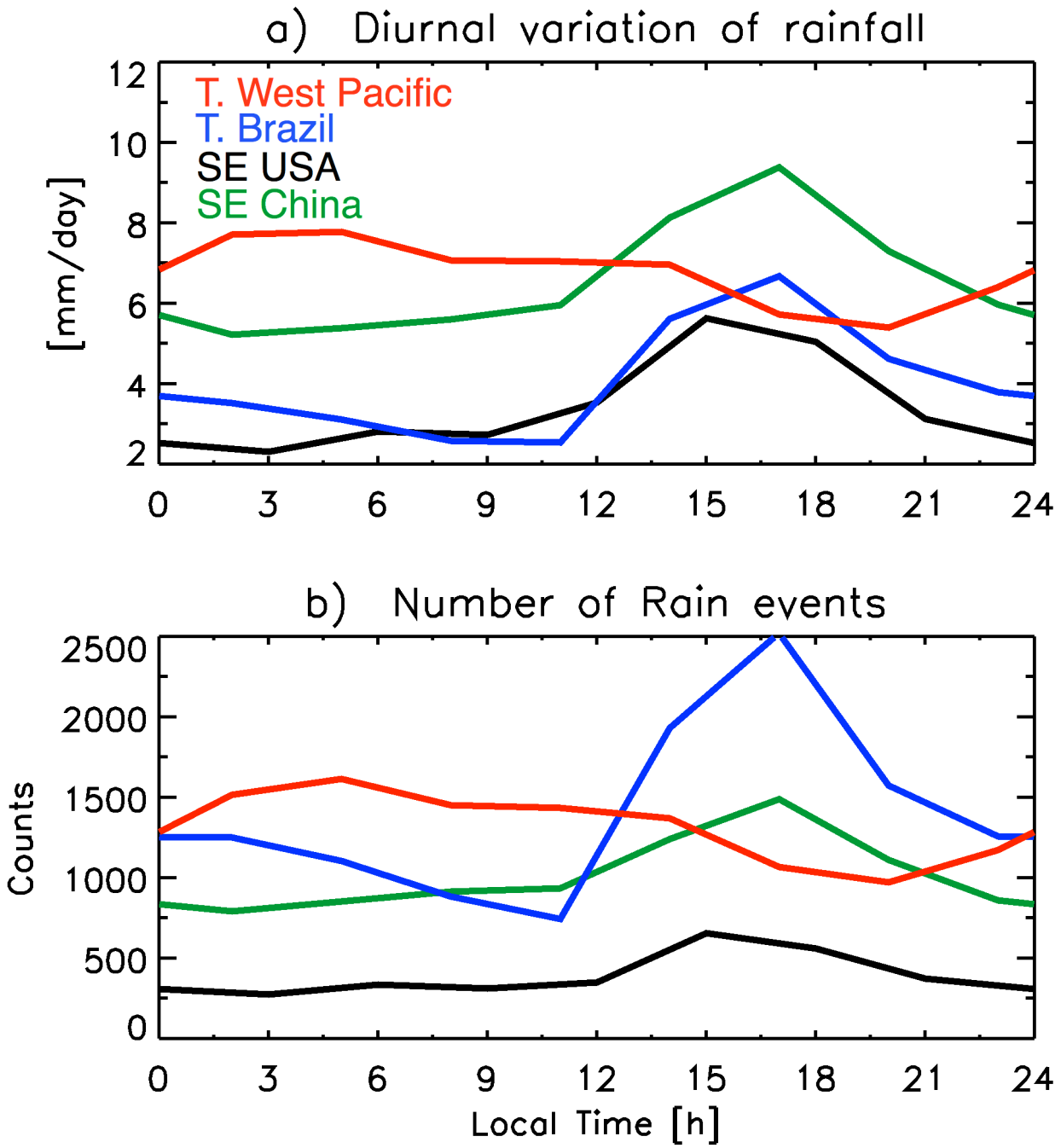

Figure 3. (a) The variation in TRMM 3B42 2x2-degree rainfall with local solar time, averaged over the radiosonde locations of each region shown in Figure 1. (b) The diurnal variation in the number of high rain events within each 3-hour time bin, calculated from all rain events used in the construction of the temperature anomaly patterns.

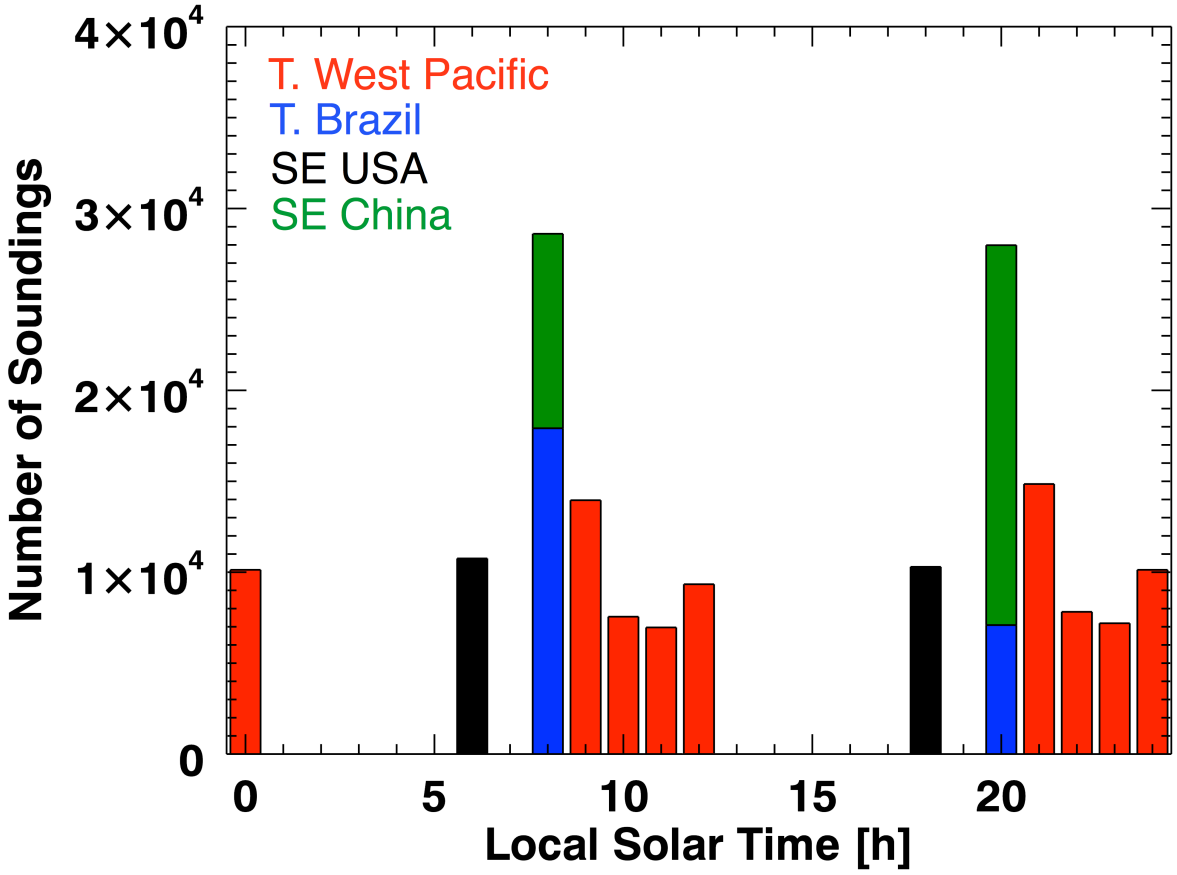

Figure 4. The number of available soundings, at each local solar time, within 48 hours of the rainfall events used in the construction of the temperature anomaly patterns. Different colors refer to different regions.

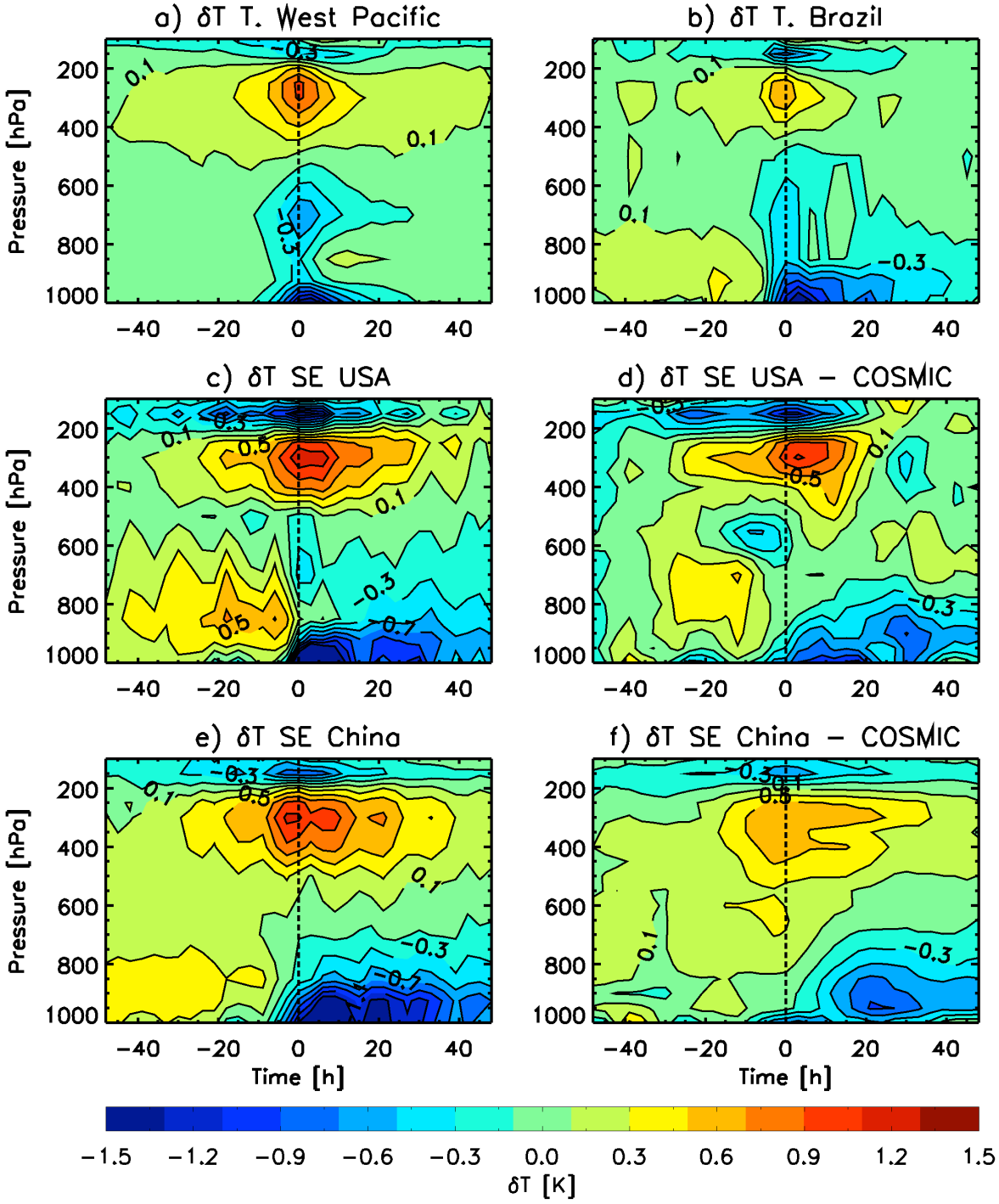

914

915 Figure 5. (a), (b), (c), and (e) show temperature anomaly patterns about the TRMM high rain
916 events, calculated using IGRA radiosonde profiles from each region. (d) and (f) show temperature
917 anomaly patterns calculated using the COSMIC GPS temperature profiles.

918

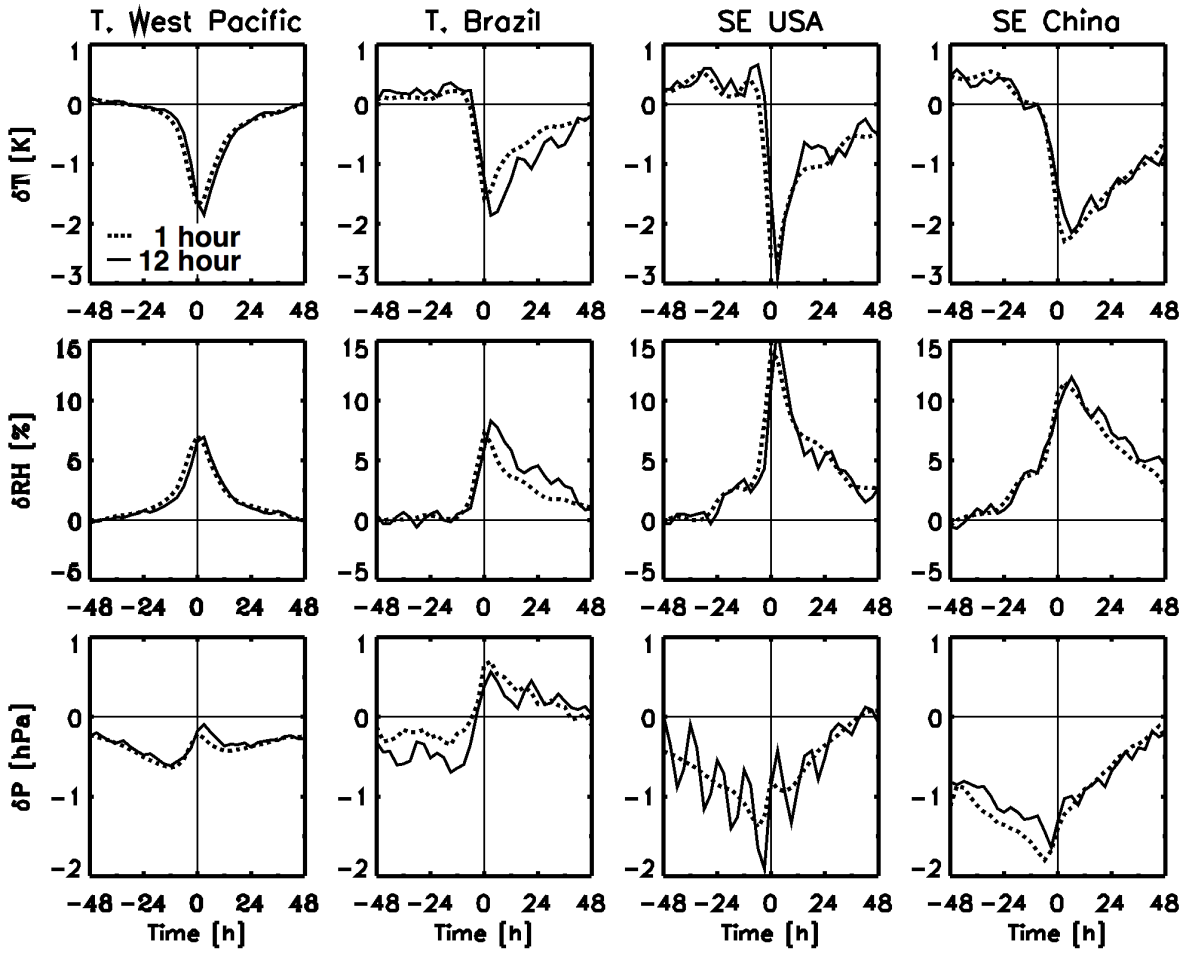

Figure 6. Within each figure, the dotted line refers to an anomaly profile calculated using 1-h ISH surface data, while the solid lines refer to anomaly profiles calculated using 12-h IGRA radiosonde data. (upper row) The variation of the surface temperature anomaly during high rain events. (middle row) The variation of surface relative humidity anomaly during high rain events. (bottom row) The variation in the surface pressure anomaly during high rain events. Each column refers to a different region with from left to right: the Tropical Western Pacific, Tropical Brazil, Southeast USA, and Southeast China regions.

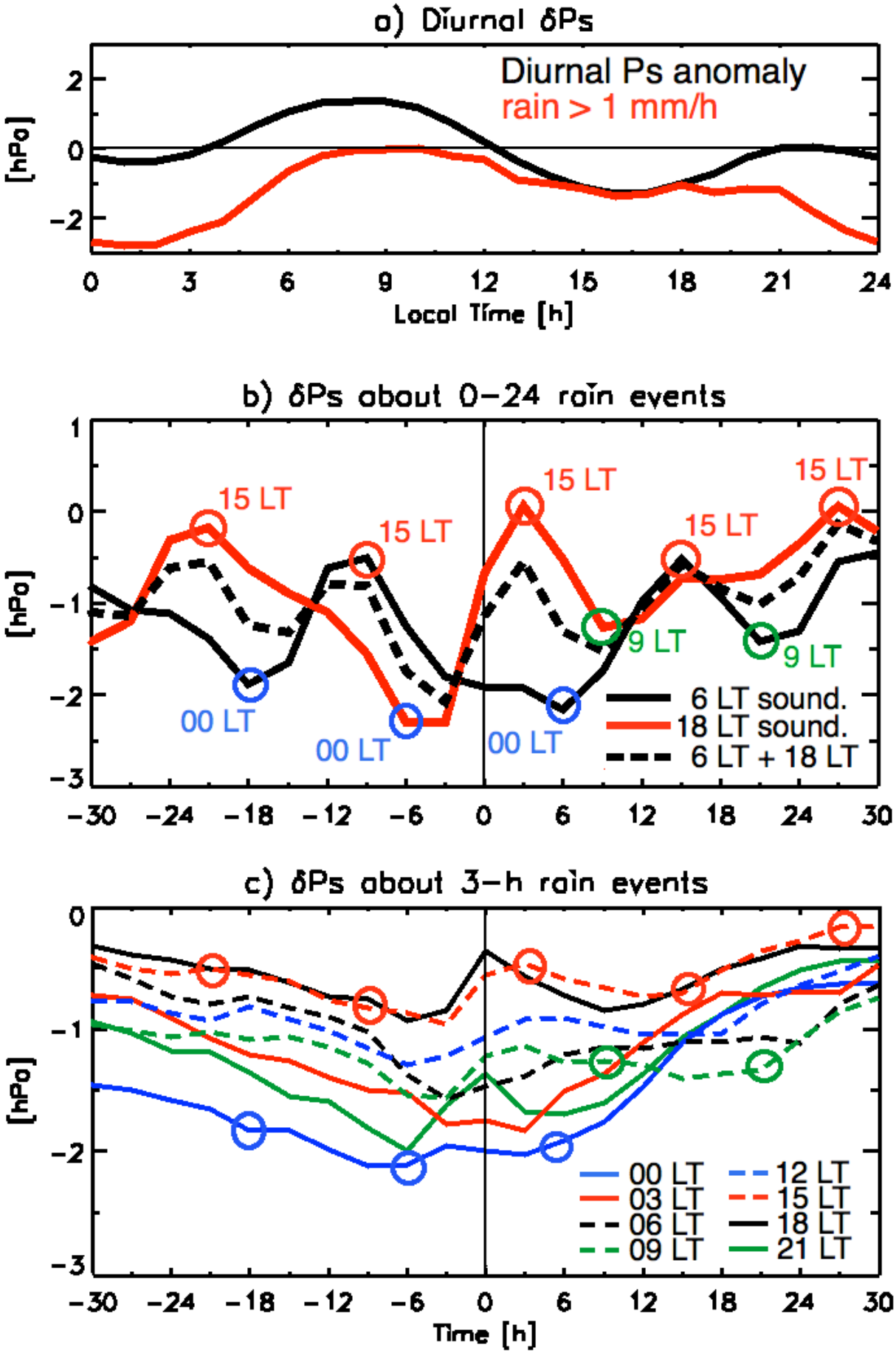
a) Diurnal δPs
Diurnal Ps anomaly
rain > 1 mm/h
[hPa]
Local Time [h]
b) δPs about 0–24 rain events
15 LT
00 LT
9 LT
6 LT sound.
18 LT sound.
6 LT + 18 LT
[hPa]
c) δPs about 3–h rain events
00 LT
03 LT
06 LT
09 LT
12 LT
15 LT
18 LT
21 LT
[hPa]
Time [h]

928

Figure 7. (a) The black curve of the top panel shows the diurnal variation in the surface pressure anomaly, plotted against local solar time, of the surface stations within the Southeast United States region shown in Figure 1 (June, July, and August). The red curve was obtained from the subset of surface pressure measurements at which the local rain rate of each surface station exceeded 1.0 mm/h; (b) The solid black curve shows the surface pressure anomaly about high rain events constructed using radiosonde measurements launched at 6 LT only. The red curve shows the surface pressure anomaly about high rain constructed from radiosonde measurements at 18 LT only. The black dashed line shows the combined surface pressure anomaly of the two radiosonde launch times. (c) Each curve shows the surface pressure response, calculated using ISH surface station data within the Southeast United States region, to TRMM rain events occurring at a particular time. For each curve, the local time of the TRMM rain events is shown in the legend. The circles in the middle panel indicate the local time of the rain events about which the pressure anomaly was calculated. For example, the red circles of the middle panel indicate surface pressure anomalies calculated from radiosondes launched at 18 LT, from rain events at 15 LT. Each red circle of the middle panel corresponds to a red circle in the lower panel, which indicates the effect of rain occurring events at that time on the surface pressure anomaly. In general, maxima in the curves of the middle panel occur at times when the corresponding rain events are associated with a smaller surface pressure anomaly, and vice versa.

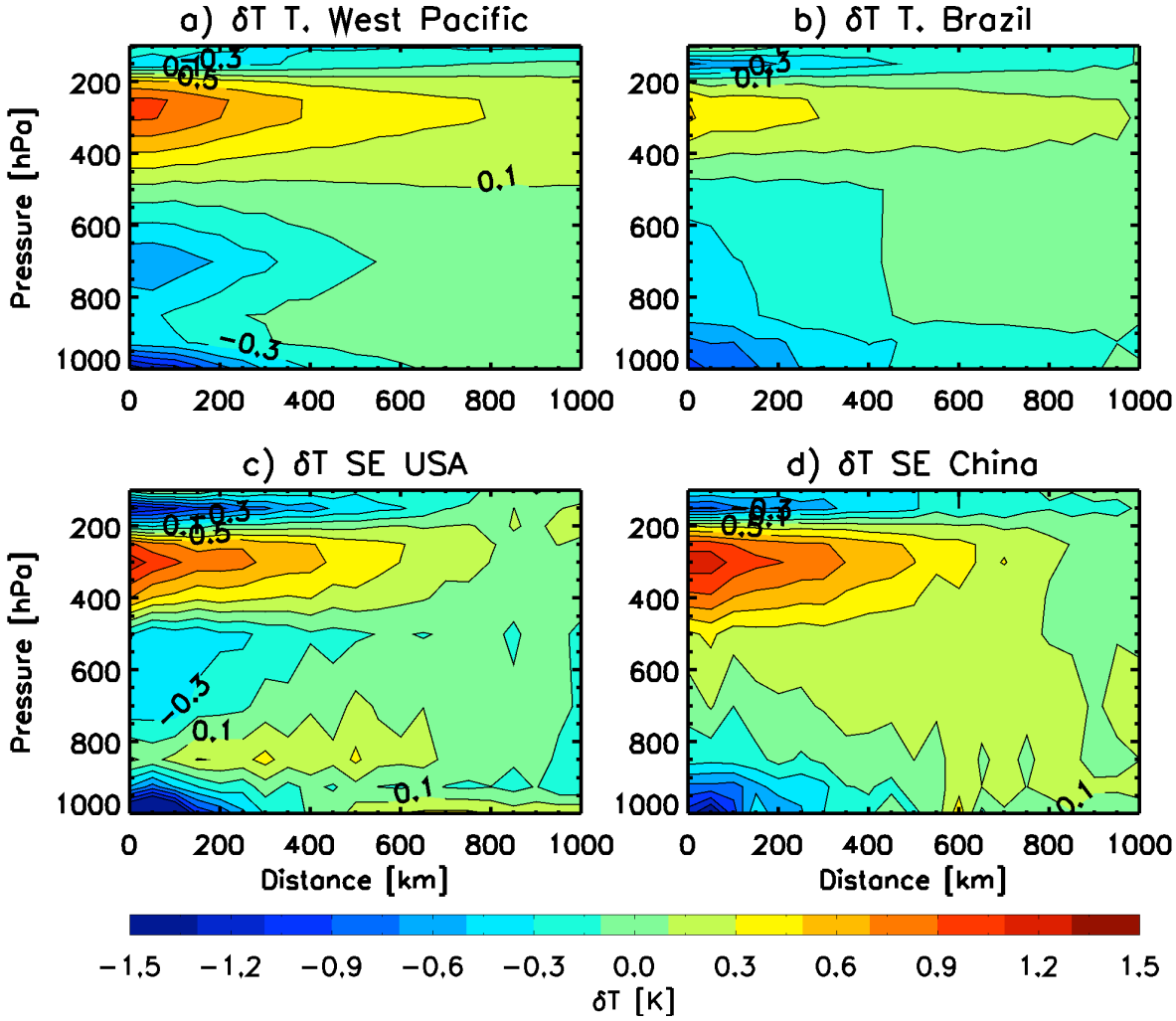

Figure 8. The radial distribution of the temperature anomaly about high rain events in each region. The horizontal axis refers to the radial distance between a radiosonde location and a TRMM high rain event. The patterns were constructed from radiosonde launches within 3 h of a TRMM rain event.

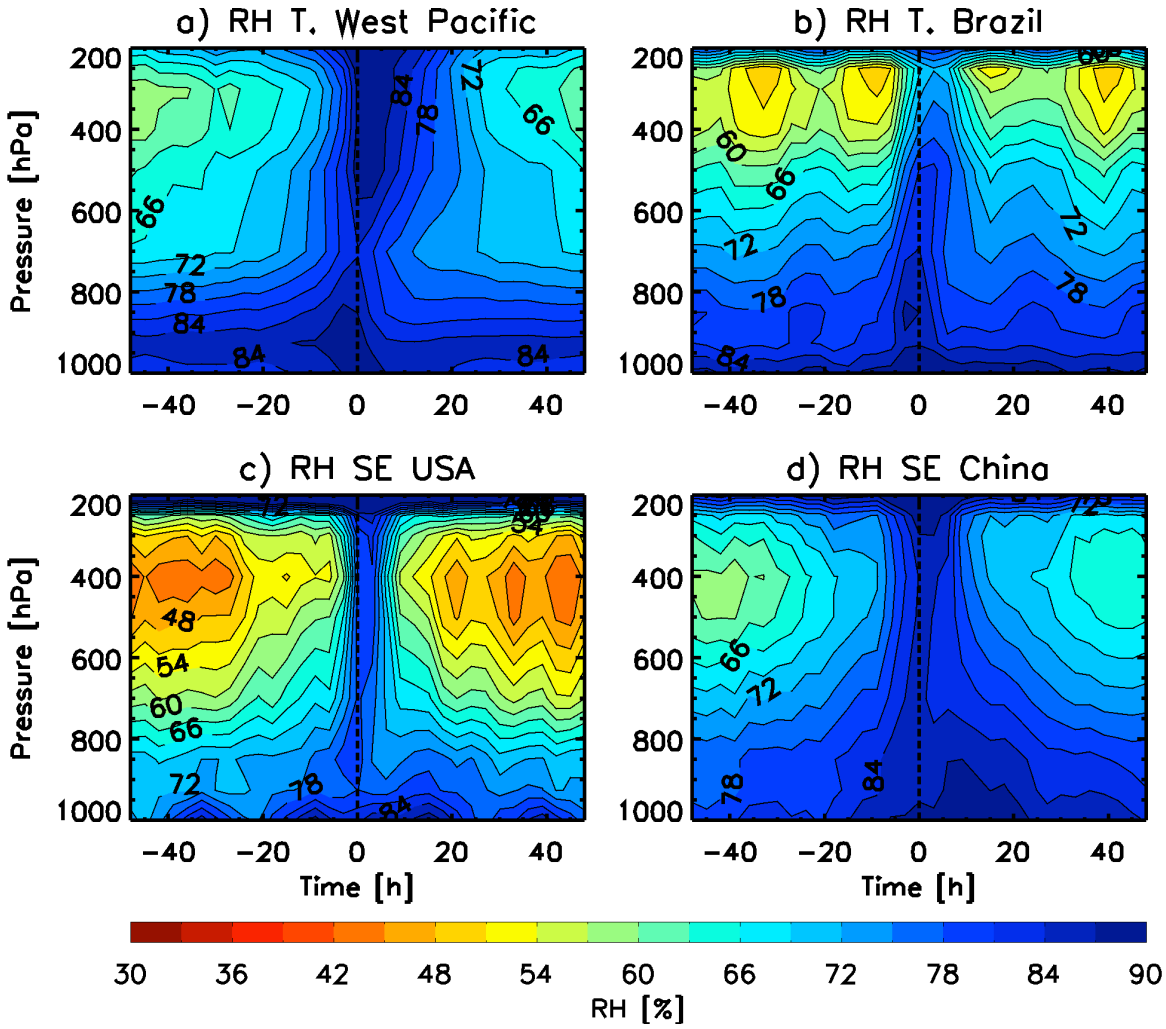

954

955 Figure 9. The variation in relative humidity during the evolution of high rain events in each region.

956 The horizontal axis refers to time since peak rainfall.

957

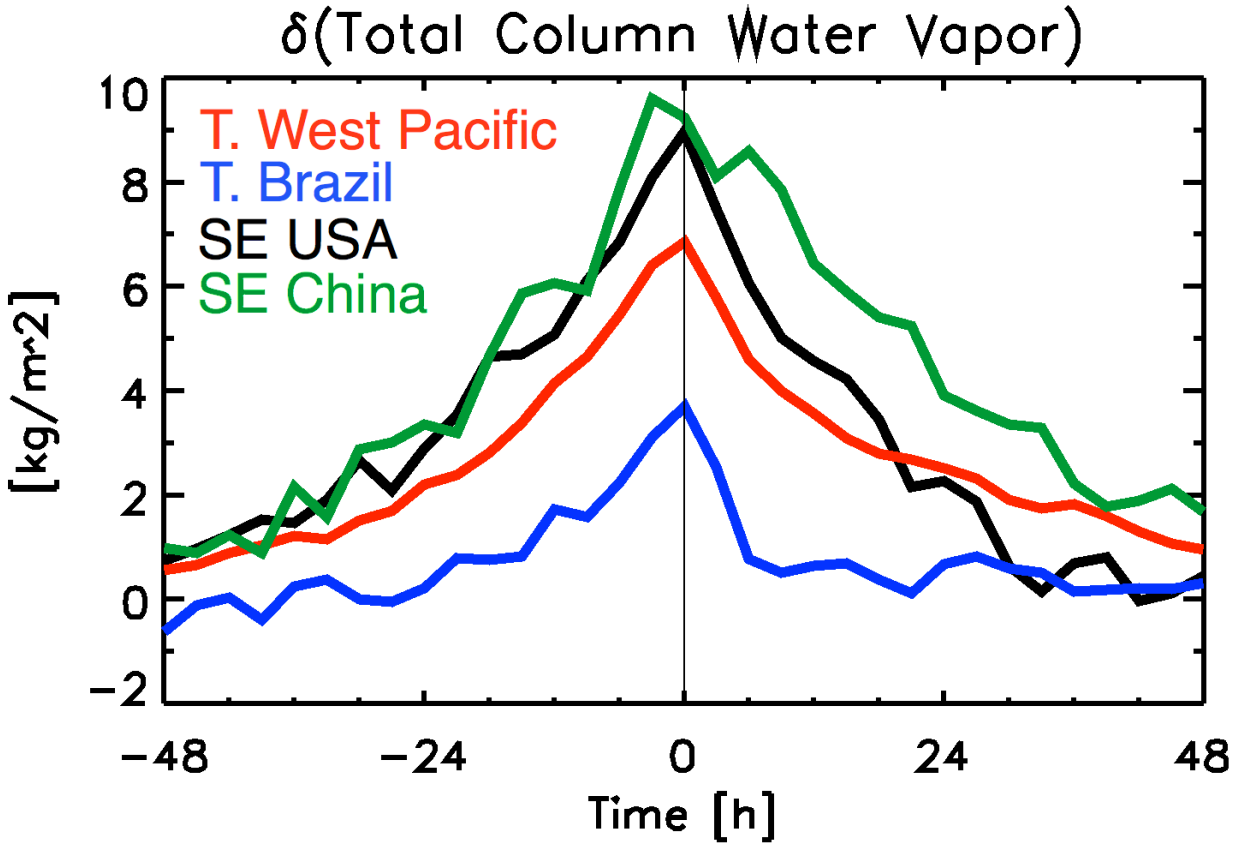

958

959 Figure 10. The variation of the total column water vapor anomaly about high rain events in each
960 region. The total column water vapor anomaly is a mass weighted vertical integral of the specific
961 humidity anomaly between 1000 and 200 hPa, as measured by a radiosonde profile.

962

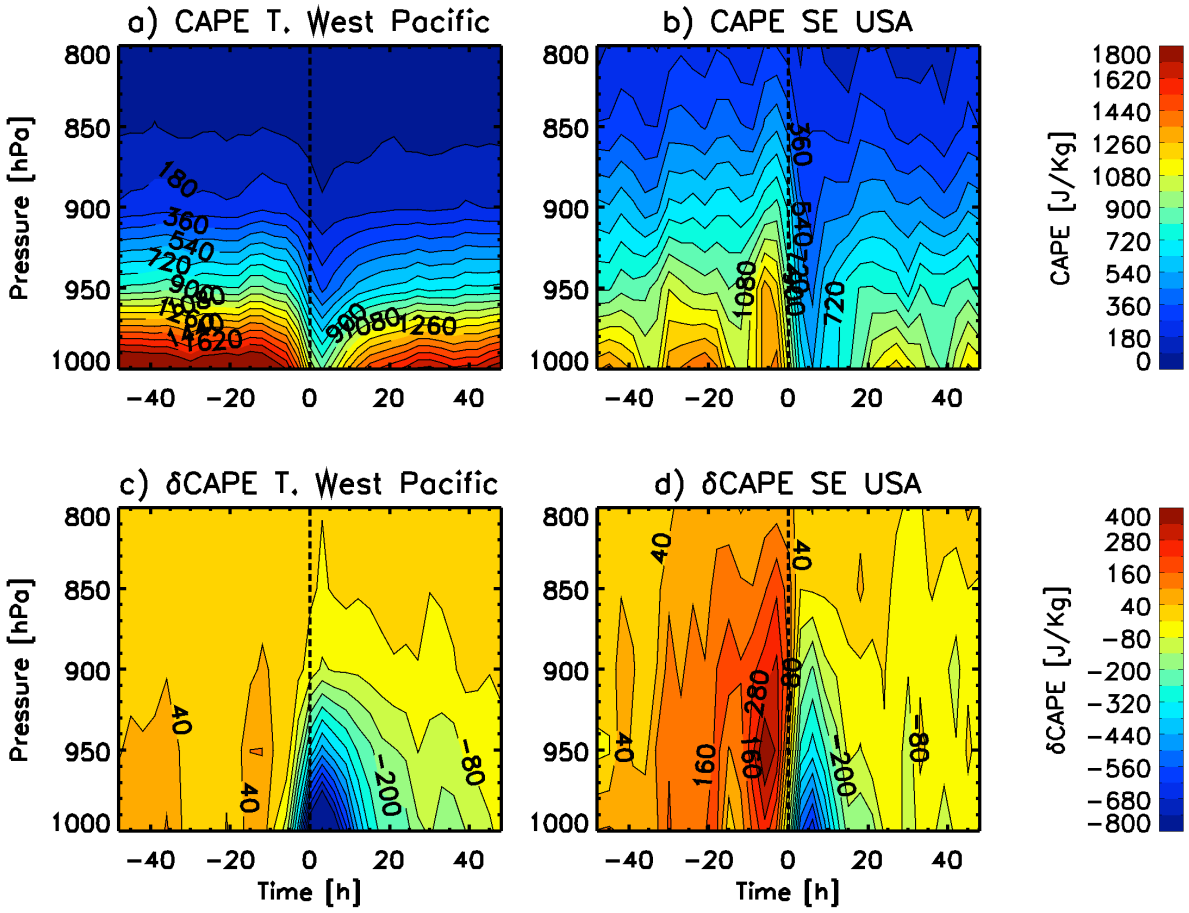

963

964 Figure 11. Panels (a) and (b) show the variation in boundary layer CAPE during high rain events in
965 the Western Tropical Pacific and Southeast United States regions. The horizontal axis refers to time
966 since peak rainfall. Panels (c) and (d) are similar to the upper panels, but show the CAPE anomaly.

967

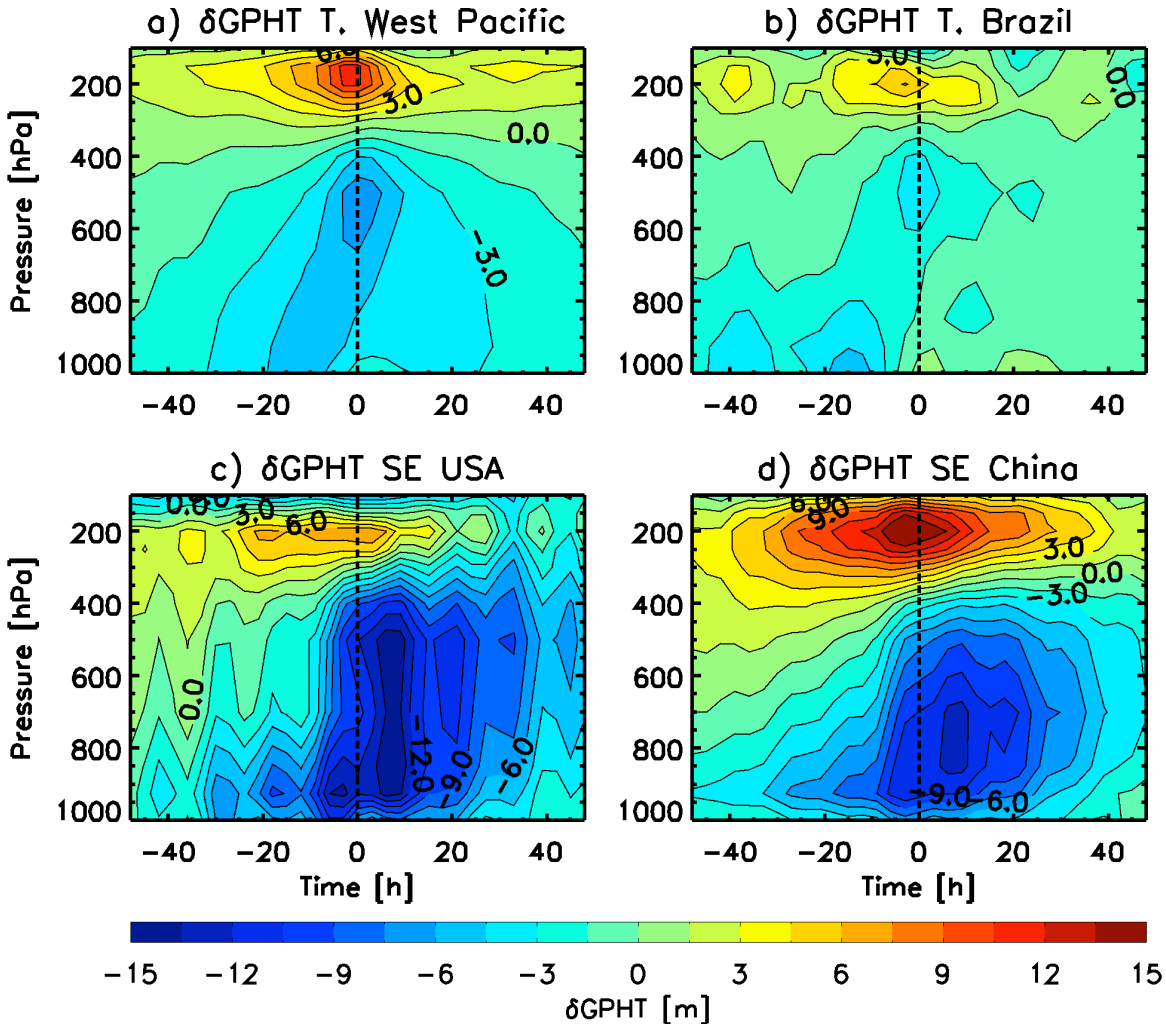

Figure 12. The variation in geopotential height (GPHT) during high rain events in each region. The horizontal axis refers to time since peak rainfall.

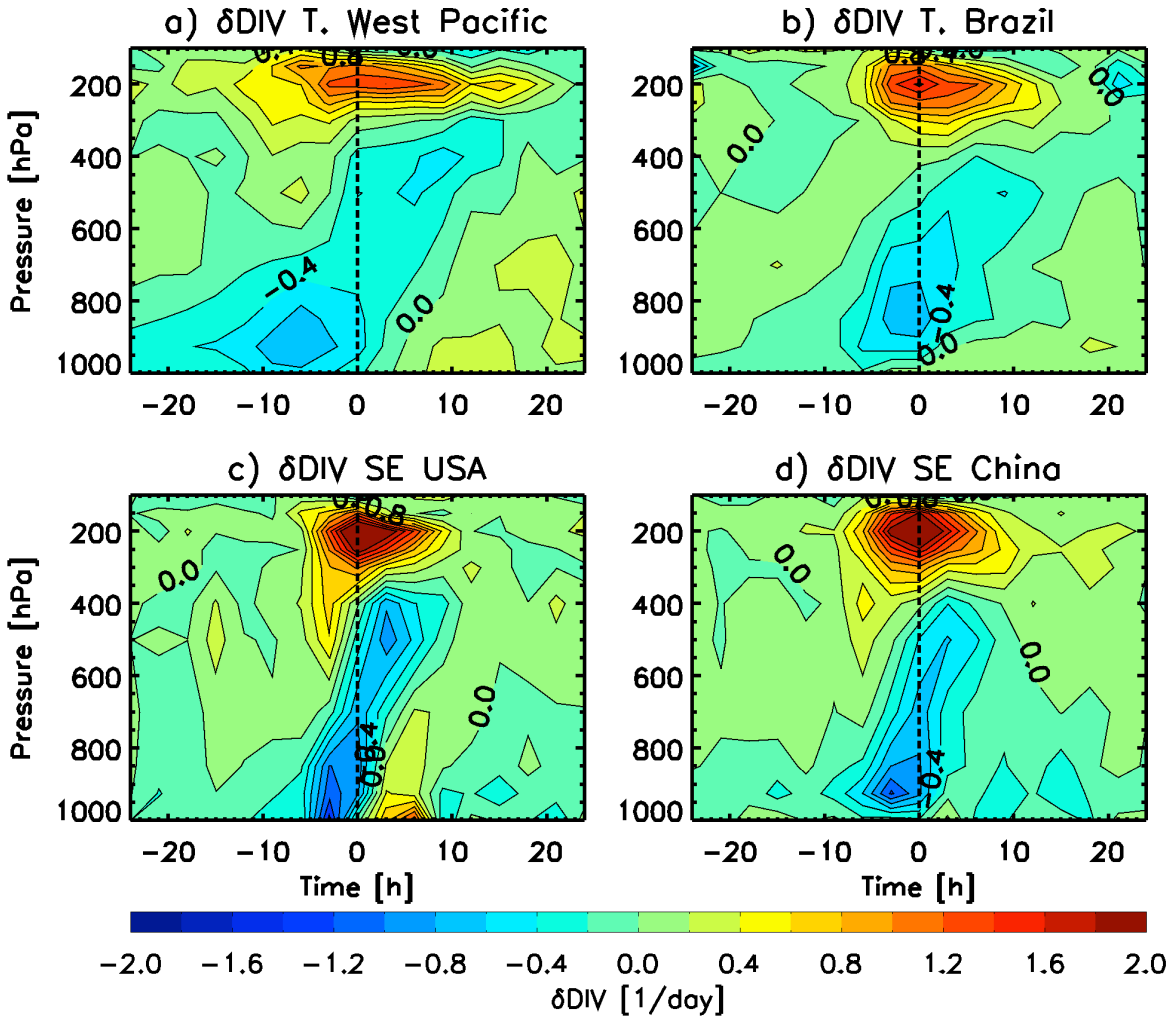

Figure 13. The variation in the mass divergence anomaly during high rain events in each region. The horizontal axis refers to time since peak rainfall.

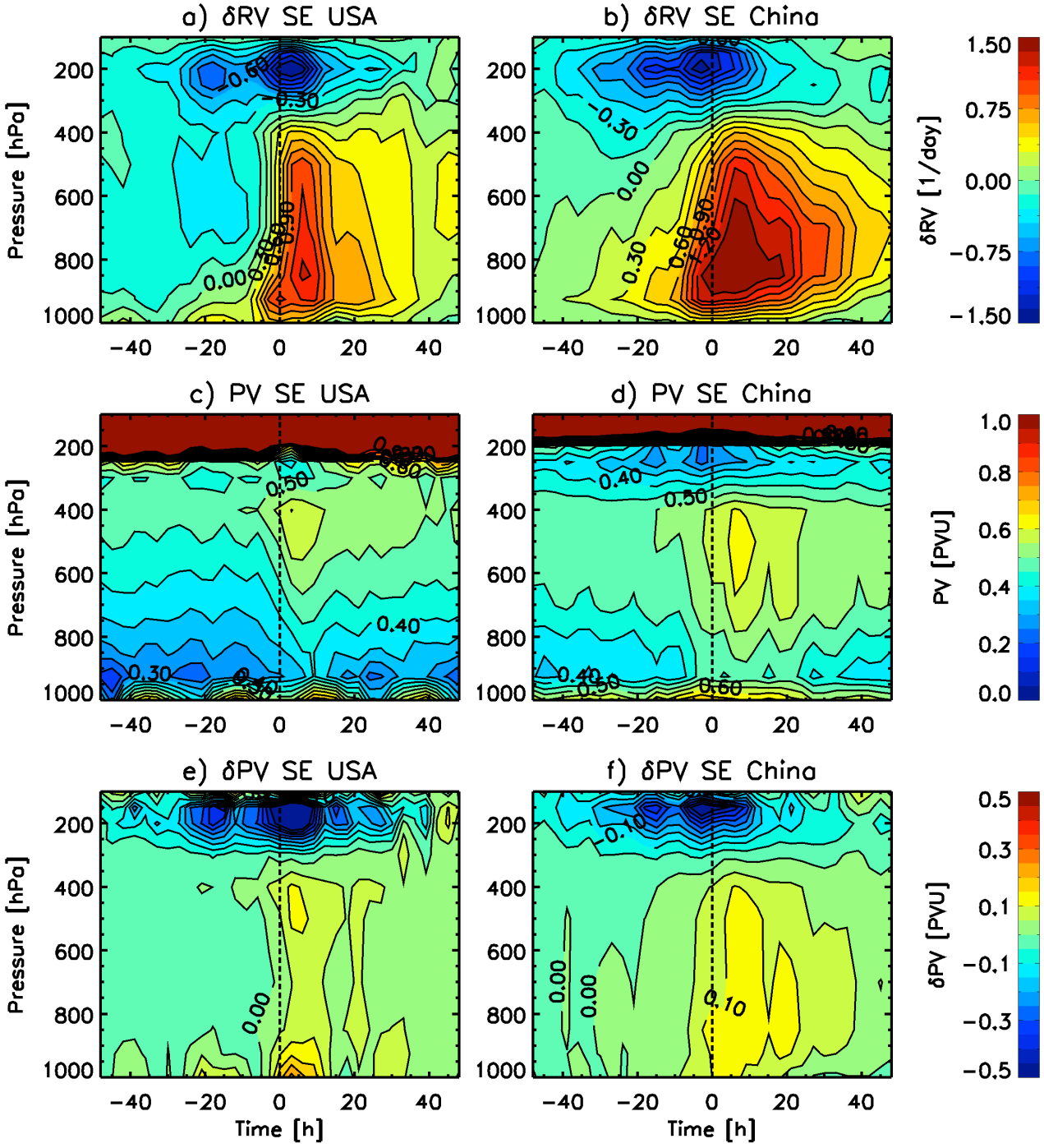

Figure 14. Panels (a) and (b) show the variation in the relative vorticity anomaly about high rain events, calculated from radiosonde arrays in the Southeast United States and China. Panels (c) and (d) show the variation in Potential Vorticity (PV) about high rain events. Panels (e) and (f) show the variation in the potential vorticity anomaly about high rain events. The horizontal axis refers to time since peak rainfall. The potential vorticity is expressed in potential vorticity units (PVU), where 1 PVU $=10^{-6} m^2 s^{-1} K kg^{-1}$.

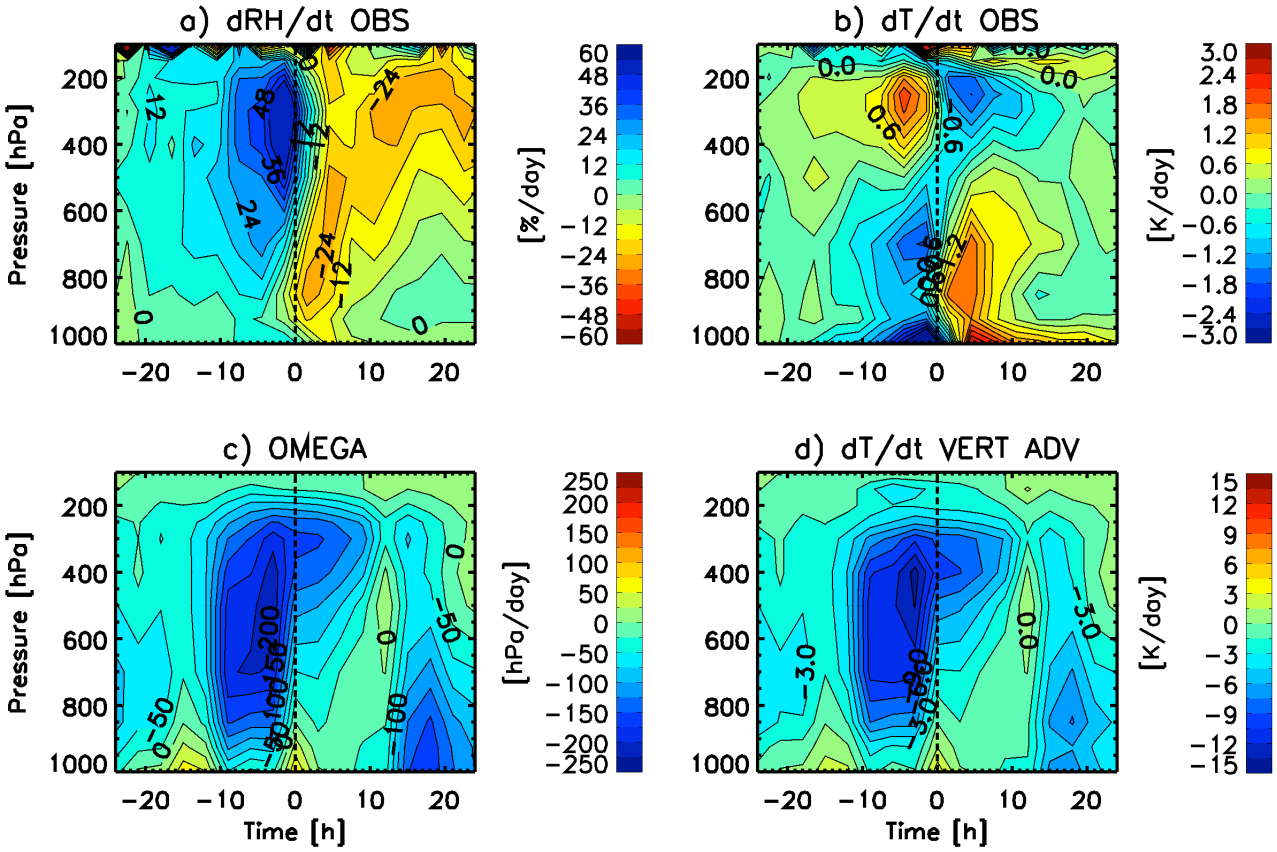

Figure 15. (a) The relative humidity tendency pattern (dRH/dt) calculated from the Western Tropical Pacific relative humidity pattern shown in Figure 9a. (b) The observed temperature tendency pattern (dT/dt), calculated from the Western Tropical Pacific temperature anomaly patterns shown in Figure 5a. (c) The vertical pressure velocity calculated from the Western Pacific divergence anomaly pattern shown in Figure 13a. (d) The temperature tendency pattern due to vertical advection, calculated from the vertical pressure velocity and stability anomaly patterns.

a) Mode-1

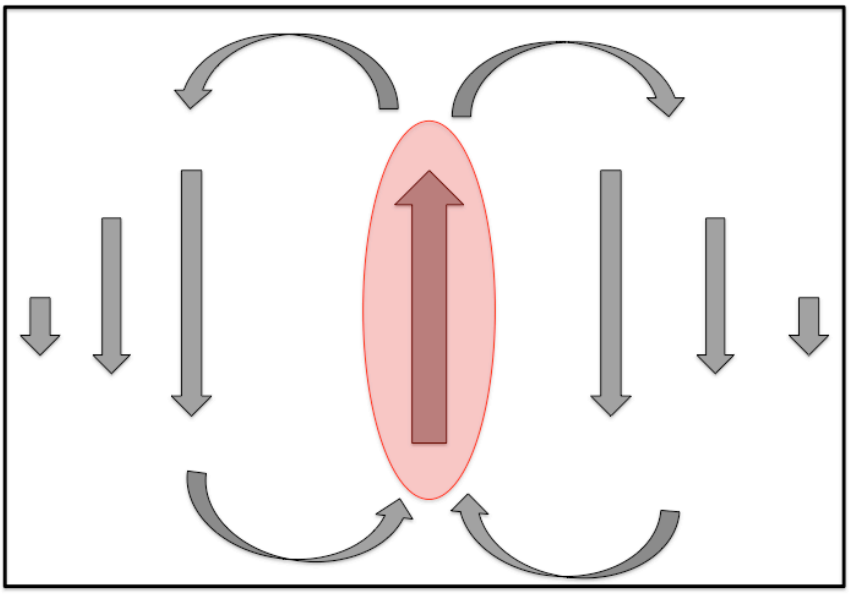

b) Rain and Column Water anomalies

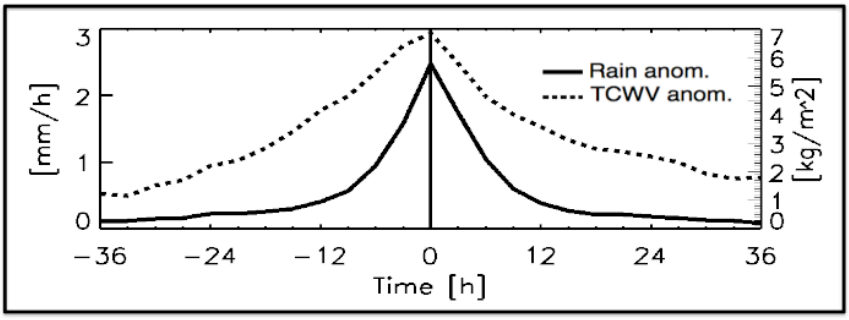

c) Mode-2

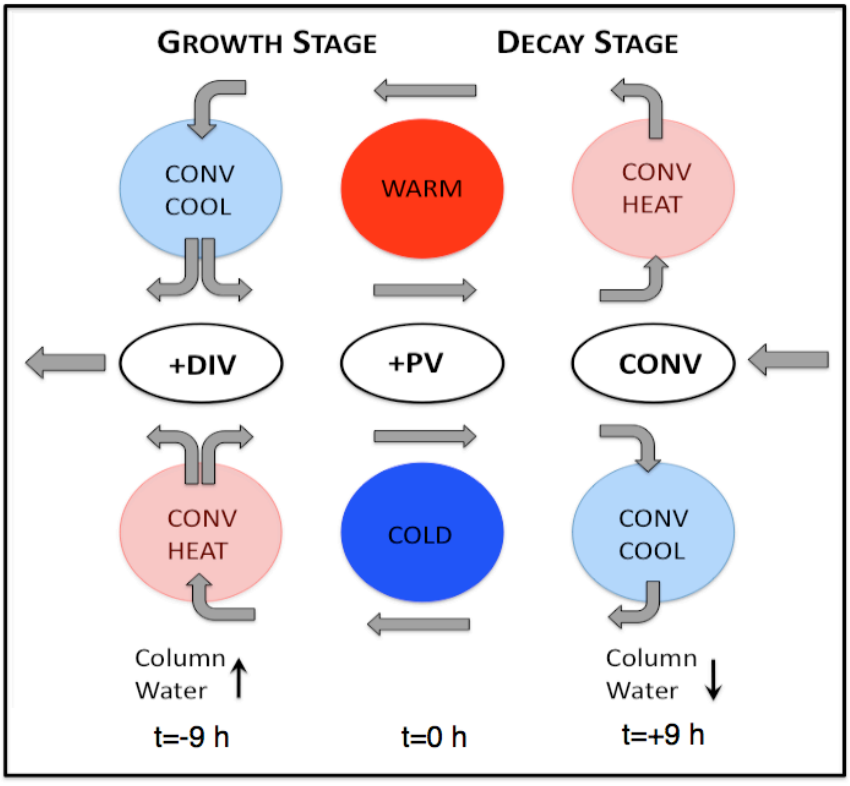

992

Figure 16. (a) The top panel shows the convective heating and large scale circulation associated with mode 1. The convective heating is indicated with the red oval, and the large-scale dynamical motions by the arrows. (b) Rainfall and column water anomalies about high rain events in Western Tropical Pacific region. (c) The convective heating and large scale circulations associated with mode 2. Dark blue and red ovals show observed cold and warm temperature anomalies. This figure has been adapted and modified from Figure 10 of Haertel and Kiladis [2004].